Available online at www.sciencedirect.com

ScienceDirect

journal homepage: www.elsevier.com/locate/he

Gas permeation through carbon membranes: Model development and experimental validation

Zançat E. Sahin [a], *Arash Rahimalimamaghani* [a], *Matteo Gazzani* [a,b], *Fausto Gallucci* [a,c,*]

[a] *Inorganic Membranes and Membrane Reactors, Sustainable Process Engineering, Chemical Engineering and Chemistry, Eindhoven University of Technology, 5600 MB Eindhoven, the Netherlands*

[b] *Utrecht University, Copernicus Institute of Sustainable Development, Princetonlaan 8a, 3584 CB Utrecht, the Netherlands*

[c] *Eindhoven Institute for Renewable Energy Systems (EIRES), Eindhoven University of Technology, PO Box 513, 5600 MB Eindhoven, the Netherlands*

HIGHLIGHTS

- Modelling of permeation through carbon membranes with a global optimization routine.
- Decreased gas permeation due to water is described with a pore-blocking model.
- Pore-size distribution used as a weight factor to sum mass transport phenomena.
- Mixture of transport phenomena for different carbon membranes predicted by model.
- Model validation with pure- and mixed gas measurements for H_2, N_2, and CO_2.

ARTICLE INFO

Article history:
Received 12 July 2023
Received in revised form
23 August 2023
Accepted 23 August 2023
Available online 09 September 2023

Keywords:
Carbon membranes
Gas separation
Mathematical modelling
Mass transport phenomena
Pore blocking

ABSTRACT

With a growing interest in carbon membranes for gas separation, understanding their performance and behaviour is essential for proper design of the membrane separation. Currently not many models exist that correctly describe transport through carbon membranes due to its complex nature. This work attempts to implement a general modelling approach which describes several key transport phenomena inside carbon membranes. The approach assumes a membrane wall to be a bundle of pores with parallel transport mechanisms using the pore size distribution as a weight factor to sum the different transport phenomena. This work adapts this approach specifically for carbon membranes, additionally accounting for molecular sieving and pore blocking effects. Imposing realistic boundary conditions, the model is solved using global optimization algorithms. For testing, four different CMSMs have been produced with hydroquinone and novolac precursors. Pure- and mixed gas permeation tests are done for these CMSMs with H_2, N_2, and CO_2 and the model is fit to this permeation data. Fitting results with pure gas measurements show the model is able to predict the contributions of different mass transport mechanism for the different membranes. This is validated by comparing these results to gas-pair perm-selectivity data. The model is furthermore fit to mixed gas data. Existence of multi-component effects shows that the model could be further improved. Overall, the model

* *Corresponding author.*
E-mail address: f.gallucci@tue.nl (F. Gallucci).

https://doi.org/10.1016/j.ijhydene.2023.08.272

presented in this work is shown to be able to describe complex mass transport behaviour for various different carbon membranes.

Nomenclature

Abbreviations

CMSM	Carbon molecular sieve membrane
PSO	Particle Swarm Optimization
SSR	Sum of squared residuals

Greek symbols

δ	Thickness m
λ	Mean free path m
μ	Dynamic viscosity Pa• s
Φ	Molar flow rate mol/s
ρ_{mol}	Molar density mol/m^3
σ_N	Standard deviation for normal size distribution m
τ	Tortuosity [–]
ϵ	Porosity [–]
φ	Molar flow rate of single capillary mol/s

Latin symbols

A	Area m^2
C_L	Langmuir isotherm coefficient [–]
C_R	Coefficient of resistance kg/(m^2 •s)
C_{ms}	Molecular sieving proportionality constant mol/(m• s • Pa)
C_{pb}	Pore blocking coefficient [–]
C_{sw}	Shape-weight factor of the specific surface 1/kg
d	Diameter m
E_{act}	Activation energy J/mol
f_{pb}	Pore blocking factor [–]
H_{ads}	Adsorption enthalpy/heat of adsorption J/mol
J	Molar flux mol/(m^2 •s)
l	Length m
M_w	Molecular weight kg/mol
N_A	Avogadro constant 1/mol
N_N	Normal pore size distribution function 1/m
n	Number [–]
p	Pressure Pa
Q_k	Rewritten normal distribution expression m^k
q_m	Adsorbed amount at full monolayer coverage mol/kg
q	Adsorbed amount mol/kg
R	Universal gas constant J/(mol• K)
r	Radius m
S_s	Specific surface area m^2/kg
T	Temperature K

Sub- and superscripts

act	Activation/active
app	Apparent
col	Collision
eff	Effective
exp	Experimental
g	Gas/gaseous
kin	Kinetic
Kn	Knudsen diffusion
max	Maximum
mem	Membrane
mol	Molar/molecule
ms	Molecular sieving
num	Numerical
pb	Pore blocking
perm	Permeate
p	Pore
ret	Retentate
slip	Slip flow
s	Surface
tot	Total
vis	Viscous flow

1. Introduction

Up to 15% of the world's energy consumption can be attributed to separation processes [1]. The global energy demand is expected to grow by 48% within the next 20 years, mainly caused by an increase in world population [2]. Separation of gasses such as H_2, CO_2, N_2, and O_2 is of global importance. Techniques such as PSA, distillation, and scrubbing dominate the current market, but membrane technology has become a growing alternative [3]. This growth is due to inherent advantages such as a high energy efficiency, small footprint, versatility in implementation, and potential fabrication costs [4,5]. Polymeric membranes are the most commonly used membranes. However, polymers cannot operate at high temperatures, many are sensitive to harsh chemical environments, and may face swelling issues. Moreover, the trade-off between permeability and selectivity described by the Robeson upper bound is a well known limit for polymeric membranes [6,7]. For these reasons there has been rising interest in developing porous inorganic membranes with potentially improved permeability, selectivity, and thermal and chemical stability. Materials with molecular sieving capabilities such as zeolites, silica, and carbon-based materials form the basis of inorganic membranes [8]. Carbon molecular sieve membranes (CMSMs) are inorganic ultramicroporous

membranes produced through carbonization/pyrolysis of a thermosetting polymer precursor under vacuum or inert conditions. They have a potential for relatively easy and low cost of production whilst maintaining both high selectivity and permeability [9]. During carbonization, the entangled polymer chains are gradually transformed into rigid carbonized aromatic strands which afterwards form organized plates [10,11]. The voids between these carbon plates (micropores) and the slits between the strands (ultramicropores) ultimately affect the permeation flux and permselectivity of the CMSM [11–14]. Their properties can therefore be fine-tuned during fabrication depending on requirements for specific separations [15]. Carbon membranes have been developed as a promising option for multiple gas purification processes such as CO_2/N_2 [16], H_2/CO_2 [17], and CO_2/CH_4 [18–20] separation.

However, not many methods currently exist to mathematically describe transport through carbon membranes [21]. Carbon membranes can have very different structures, as many variables affect the pores and the functional surface groups. These in turn result in different transport phenomena. While this might be advantageous for fine-tuning, it makes it challenging to capture transport behaviour in a uniform model. A few phenomenological methods exist in literature. One option is the solution-diffusion model, as discussed by Ismail et al. [9]. Notably, it groups all transport phenomena into a single permeation term, simplifying the system. For binary systems in carbon membranes, Fick's law can be used as shown by Gilron and Soffer [22]. They developed two models where mass transport mechanisms are assumed to occur either in parallel within the pores or in series as the pore changes in width along the length. When fitting permeance data at different temperatures, they found that the resistance-in-series model predicted the results better. Works on multi-component systems use the Maxwell-Stefan equation or the Dusty-Gas Model to describe the transport through the pores [10,23–26]. This has however proven to be challenging. The Dusty-Gas Model does not include activated (configurational) diffusion, which is the main transport mechanism for CMSMs. Furthermore, finding accurate values for Maxwell-Stefan diffusion coefficients in multi-component systems can be challenging [27].

Rangarajan et al. proposed an interesting phenomenological approach for describing pure gas permeation through asymmetric porous membranes [28]. It takes into account that the membranes do not have uniform pore sizes, but rather a pore size distribution. Therefore, the contribution of each mass transport mechanism is linked to the pore structure via a weight factor. This was adapted by Li to ceramic membranes and carbon membranes [29]. More recently, Pirouzfar and Omidkhah further implemented a genetic algorithm to fit this model to experimental data for a CMSM with a sum squared error function for the permeability [30]. While the methodology is promising, they lump their fitting parameters together. The link between transport behaviour inside these membranes and model becomes less clear, decreasing the physical relevance and applicability of the model. Aside from these phenomenological approaches, molecular simulation is another interesting field for carbon membrane. Few works have applied molecular simulation methods to carbon membranes [31–36].

This work contributes to the modelling of gas separation and mass transport inside carbon membranes by providing a general modelling approach. This approach takes into account and couples the relevant phenomena present in carbon membranes. Starting from Rangarajan's approach extended by Li [29] and Pirouzfar and Omidkhah [30], we extend the implementation for gas separation in carbon membranes with the following key novelties. Firstly, we provide a global fitting procedure which allows for realistic physical limits in the model. Secondly, molecular sieving is taken into account with a separate flux term. Lastly, pore-blocking at low temperatures and pressures caused by the presence of water molecules is implemented using a pore-blocking factor. The model is fit and validated for several pure gas- and multi-component tests (H_2, N_2, and CO_2) in four different CMSMs produced within the research group. The tested membranes each have different characteristics and mass transport behaviour based on their fabrication parameters. We show that the model is able to predict the different transport behaviour (e.g. molecular sieving, Knudsen diffusion) per membrane and permeating gas. While modelling in this work focuses on CMSMs, the developed methodology is in principle applicable to a wide range of carbon membrane applications. The paper is organized as follows; section 2 describes the mathematical model and its underlying assumptions, section 3 discusses the membrane synthesis and permeation tests, section 4 describes modelling results, and section 5 is the conclusion.

2. Mathematical model

Within the field of flow through porous media, the pore dimensions play a crucial role in the type of transport mechanism that will dominate. The pore dimensions and gas densities within those pores affect the rate of particle-particle collisions with respect to particle-wall collisions. These in turn influence the characteristics of the prevailing transport mechanisms. The frequency of these collisions is often described using the mean free path (λ), defined as the average length a particle travels between collisions.

Based on characteristic ranges of the Knudsen number, defined as $\mathrm{Kn} = \lambda/d_p$, three to four flow regimes are generally recognized. In an increasing degree of rarefaction, i.e. increasing *Kn*, these four flow regimes are respectively denoted as “continuum flow”, “slip flow”, “transition flow”, “free molecular flow” [37]. Sometimes “slip flow” and “transition flow” are lumped together into a single flow regime. Fig. 1 gives a qualitative representation of the flow regimes in porous media, as a function of a “packing density” (y-axis) and kinetic radius of the permeating molecules relative to the pore radius (x-axis). The smallest mean free path is achieved at the highest molar density and highest permeating molecule radius relative to the pore radius. As either the molar density or the molecule size decreases, particle-particle interactions decrease relative to particle-wall interactions, resulting in a shift in flow regime. At nanopore level, where the pores start to reach the size of the molecules themselves, activated

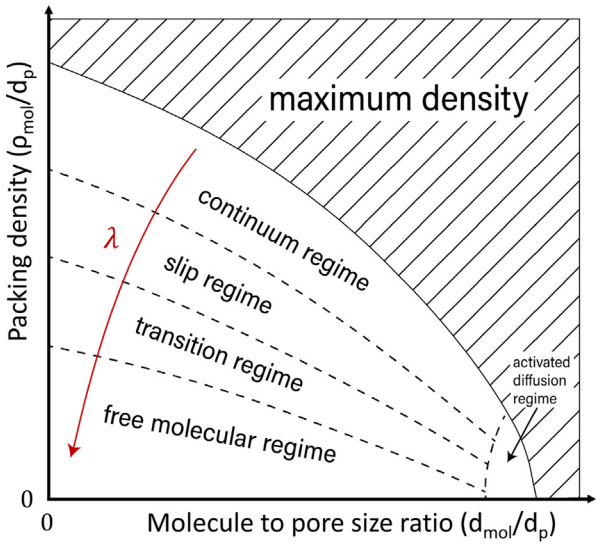

Fig. 1 – Schematic representation of flow regimes in porous media as a function of packing density and molecule size relative to pore size [21]. The precise shape and proportions of the flow regimes are a function of the properties of the fluid and the system.

diffusion effects start to play a role. Within carbon membranes, generally the following 7 transport mechanisms can be found:

1. Viscous flow and/or molecular diffusion for continuum fluid transport;
2. Transition- and slip flow in the transition and slip regime where slip effects on the pore walls occur;
3. Knudsen diffusion in the free molecular regime where particle-wall collisions govern the transport;
4. Surface diffusion where molecules move along a surface through adsorption and desorption processes;
5. Capillary condensation where the partial pressure of a condensable permeating component is sufficient to facilitate condensation inside the porous network;
6. Activated diffusion (also referred to as configurational diffusion or molecular sieving) where pore dimensions start approaching molecule sizes. Interaction potentials overlap considerably, creating a much stronger potential for trapped gas molecules which introduces a series of activation barriers which the molecules must overcome [38,39];
7. Solution-diffusion through a dense solid layer where transport of particles is considered to go through transient gaps within the solid matrix rather than through a porous network;

The transport behaviour inside carbon membranes depends on several factors, most notably the conditions during pretreatment, synthesis, and post-treatment. For example, important variables are the chosen precursors, carbonization temperature, heating rate, atmosphere and thermal soaking time of the membrane in the chosen atmosphere during carbonization. Other minor variables are flow rate and pressure [3,9]. Moreover when selecting ideal precursors, properties such as chemical structure, glass transition temperature, and fractional free volume should be considered carefully [14,40,41]. All these parameters give ample design margins to fine-tuned carbon membranes according to specific separations and reactions, facilitating the separation of challenging mixtures such as H_2/CO_2 and alkenes/alkanes [14,15]. An example of such tuning is shown in Llosa et al. where the permselectivity-permeance characteristics were adjusted by fine-tuning the pyrolysis temperature [42]. Moreover, during operation, several factors can modify the transport behaviour inside carbon membranes; concentration polarization, fouling and pore blocking effects, membrane rupture and deterioration at harsh conditions, reaction of surface functional groups. This adds complexity and should be carefully considered when trying to model and describe transport inside these membranes.

2.1. *Parallel resistance model*

In order to describe the different mechanisms of transport through carbon membranes, the pore structure can be represented as a bundle of parallel capillary tubes with a size (diameter) distribution. The type of transport mechanism becomes therefore a function of the pore size using the distribution as a weighing factor. This determines to what degree each mechanism contributes to transport and which mechanism dominates at certain conditions. Carbon membranes for gas separation purposes will generally operate in an activated diffusion regime (e.g. CMSMs). Supports for such CMSMs will generally be in a free molecular regime showing Knudsen diffusion. Liquid applications will generally operate in a continuum or transition regime depending on the specific pore size, morphology, and application. This was first proposed for pure gas permeation by Rangarajan et al. [28], and has later been adapted by Li [29] and Pirouzfar and Omidkhah [30]. In this work, we further improve the model. The main assumptions of the model are as follows.

1. The (nano)porous membrane consists of a bundle of parallel capillaries with a normal size distribution given by equation (1). For a given membrane, moderate temperature and pressure fluctuations are assumed to have negligible influence on this mean pore radius and standard deviation. The pore size distribution is therefore constant for a given membrane, for conditions at which the structural integrity of the membrane is not challenged.

$$N_N(r) = \frac{n_p}{\sqrt{2\pi}\sigma_N} \cdot \exp\left[-\frac{1}{2}\left(\frac{r-\bar{r}}{\sigma_N}\right)^2\right] \quad (1)$$

2. Transport inside the pores occurs as a result of (i) a pressure gradient along the thickness of the membrane and (ii) adsorption and desorption equilibria at the pore internal surface. The equilibria are assumed faster than the overall transport rate, therefore neglecting adsorption and desorption kinetics. It results that the permeating molecules can be either in gaseous- or in adsorbed form.
3. Transport outside the pores is faster than transport in the pores; any external transport effects (e.g. concentration polarization, transport through support layer) are negligible.
4. The exchange of molecules between the gaseous and adsorbed species can be neglected inside the membrane

during permeation from retentate-to permeate side. The pressure gradient is assumed to be linear for any position inside the membrane.

5. The diameter of each individual capillary is assumed to remain constant along its length. This means that the weight factors for each mechanism are assumed to remain constant along the length of the capillary, thus along the thickness of the dense membrane layer. This effectively eliminates any resistance-in-series type of addition of the mechanisms.
6. The non-ideal geometry of the porous structure is accounted for by a porosity ϵ and tortuosity τ.
7. Transport through the transient gaps of the solid carbon matrix is negligible compared to transport through the pores [9,43]. Therefore solution-diffusion is neglected with respect to the other transport mechanisms.
8. Capillary condensation and critical capillarity effects are neglected. This work considers permeation of simple non-condensable gases (H_2, N_2, and CO_2), which are not easily prone to capillary condensation.

The resulting parallel resistance model builds upon a single total molar flux which is given by a sum of the gaseous and surface transport. Fig. 2 provides a schematic equivalent layout of the model.

$$J_{tot} = J^{g}_{tot} + J^{s}_{tot} \tag{2}$$

The different terms found in J^{g}_{tot} and J^{s}_{tot} need to be defined. The gaseous mass transport through carbon membranes can be written by adding all relevant gaseous mass transport mechanisms, namely viscous flow, slip flow, Knudsen diffusion, and molecular sieving. Each mechanism is weighted with the pore size distribution and calculated over the relevant radius domain, resulting in the following expression [28,29]:

$$\begin{aligned}\Phi^{g}_{tot} &= \Phi_{vis} + \Phi_{slip} + \Phi_{Kn} + \Phi_{ms} \\ &= \int_{r=r^{low}_{vis}}^{r^{high}_{vis}} N_N(r)\varphi_{vis}(r)\,dr + \int_{r=r^{low}_{slip}}^{r^{high}_{slip}} N_N(r)\varphi_{slip}(r)\,dr \\ &+ \int_{r=r^{low}_{Kn}}^{r^{high}_{Kn}} N_N(r)\varphi_{Kn}(r)\,dr + \int_{r=r^{low}_{ms}}^{r^{high}_{ms}} N_N(r)\varphi_{ms}(r)\,dr\end{aligned} \tag{3}$$

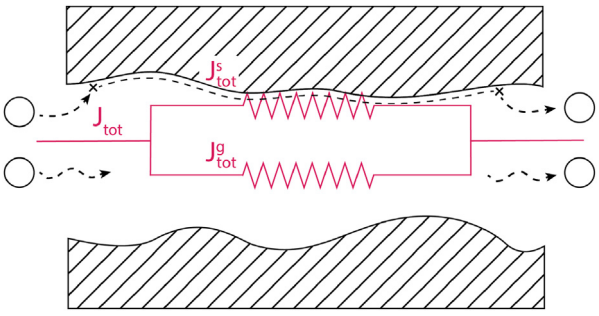

Fig. 2 – Schematic representation of mass transport through pores using the parallel resistance model, depicting gaseous- and surface transport in parallel.

where Φ is the total molar flow through the membrane and φ is the molar flow through a single pore. The mean pore area is equal to the total membrane area divided by the number of pores and it can be approximated as follows:

$$\frac{A_{mem}}{n_p} \cong \frac{\pi \bar{r}_p^2}{\epsilon} \tag{4}$$

Note that this single mean pore area takes into account the porosity, accounting for the solids around the pores. The molar flow in a single pore i (φ_i) can therefore be written in terms of molar flux, where J_i will differ per transport mechanism.

$$\varphi_i \cong \frac{\pi r_{p,i}^2}{\epsilon} J_i \tag{5}$$

Within macropores, continuum fluid transport can be described as a combination of molecular (bulk) diffusion and viscous (Poiseuille) flow. Under such conditions, molecular diffusion is less than 1% of the viscous flow so it can be neglected [44]. Viscous flow driven by a pressure gradient can be described by the Hagen-Poiseuille law for a Newtonian fluid in laminar flow through a cylindrical tube with a constant cross-section. Introducing porosity (ϵ) and tortuosity (τ) for the membrane pore structure, viscous flow can be written in terms of an effective molar flux. Here, $\bar{p}$ is the mean pressure along the active layer thickness of the membrane.

$$J^{eff}_{vis} = \frac{\epsilon r_p^2}{\tau 8\mu} \frac{\bar{p}}{RT} \frac{\Delta p}{\delta^{act}_{mem}} \tag{6}$$

At higher Knudsen number, molecules near the pore wall will slip, leading to a slip- and transition flow regime. Less molecules are trapped near the wall due to rarefaction, which reduces the collision frequency of these trapped molecules. Similarly for this regime, here denoted as slip flow, the molar flux can be defined as follows ([45,46] as cited by Ref. [29]):

$$J^{eff}_{slip} = \frac{\epsilon r_p}{\tau} \sqrt{\frac{\pi}{8RTM_w}} \frac{\Delta p}{\delta^{act}_{mem}} \tag{7}$$

As pore dimensions go to the mesopore scale and the Knudsen number becomes even larger, particle-wall collisions dominate particle-particle collisions and Knudsen diffusion becomes the most prevalent mass transport mechanism. Effective Knudsen diffusion can be described as follows ([47] as cited by Ref. [29]):

$$J^{eff}_{Kn} = \frac{\epsilon r_p}{\tau} \sqrt{\frac{32}{9\pi RTM_w}} \frac{\Delta p}{\delta^{act}_{mem}} \tag{8}$$

When pore dimensions are approaching molecule sizes, activated diffusion (or configurational diffusion) occurs. Within this pore size range, separation occurs thanks to molecular sieving where certain molecules are too big to pass through the pores. Diffusion within this regime is a strong function of molecular size and shape, pore size and shape, as well as interactions between the molecules and the pore wall [29]. While we model molecular sieving as a gaseous transport mechanism, the pores are so small that no distinction can be made between molecules travelling through gaseous transport and adsorbed molecules travelling through surface

diffusion [48]. Interaction potentials overlap considerably, creating a much stronger potential for trapped gas molecules [38,39]. Restrictions by the pore wall introduce a series of activation barriers which the molecules must overcome. The diffusivity is therefore predominantly affected by the kinetic diameter for activated diffusion [49]. An extremely high permselectivity can be reached in this regime, with possibility of separation at size differences as little as 0.02 nm [50]. Activated diffusion can be described with a form of Fick's law per chemical species j, making use of Henry's law for solubility and an Arrhenius type of expression for both the solubility and diffusivity expression [22,29]. The expression is as follows:

$$J_{ms,j} = C_{ms,j}\exp\left(-\frac{E_{act,ms,j}}{RT}\right)\frac{\Delta p_j}{\delta_{mem}^{act}} \tag{9}$$

where C_{ms} is a temperature independent proportionality constant defined as a product of the proportionality constants for solubility and diffusivity ($C_{ms} = D_0 S_0$) and the activation energy $E_{act,ms}$ is a combination of the transport activation energy and heat of adsorption [22,29].

Combining equations (1), (3)–(5) and inserting all defined flux equations (eqs. (6)–(9)) gives

$$J_{tot}^{g} = \sqrt{\frac{\pi}{2}}\frac{n_p}{\sigma_N A_{mem}}\frac{\Delta p}{\delta_{mem}^{act}}\cdot\left[\int_{r_{vis}^{low}}^{r_{vis}^{high}} Q_4(r)\frac{\bar{p}}{8\mu RT\tau}dr + \int_{r_{slip}^{low}}^{r_{slip}^{high}} \frac{Q_3(r)}{\tau}\sqrt{\frac{\pi}{8RTM_w}}dr + \int_{r_{Kn}^{low}}^{r_{Kn}^{high}} \frac{Q_3(r)}{\tau}\sqrt{\frac{32}{9\pi RTM_w}}dr + \int_{r_{ms}^{low}}^{r_{ms}^{high}} Q_2(r)C'_{ms}\exp\left(-\frac{E_{act,ms}}{RT}\right)\right] \tag{10}$$

where

$$Q_k(r) = r^k\cdot\exp\left[-\frac{1}{2}\left(\frac{r-\bar{r}}{\sigma_N}\right)^2\right] \tag{11}$$

Note that $C'_{ms} = C_{ms}/\epsilon$. It follows that only $Q_k(r)$ is dependent on the pore radius r_p. This expression is a Gaussian integral which we can solve algebraically. By considering the limit $\lim_{r\to\infty}(\int Q_k(r)dr) = 0$, the integration constant is derived to be $c = \sigma_N\cdot b\sqrt{\frac{\pi}{2}}$. The resulting integral expression has the following generic form for at least $k \leq 4$.

$$\int Q_k(r)dr = -\sigma_N\left[\sigma_N a_k\cdot\exp\left[-\frac{1}{2}\left(\frac{r-\bar{r}}{\sigma_N}\right)^2\right] + b_k\sqrt{\frac{\pi}{2}}\cdot\left(\mathrm{erf}\left[\frac{\bar{r}-r}{\sigma_N\sqrt{2}}\right]-1\right)\right] \tag{12}$$

Parameters a and b are reported in Table 1, for $k\in$ [0,4].

The transition points (Table 2) between transport mechanisms are a function of the material properties, pore size distribution, operating conditions, and inlet composition [51]. The following transition points and heuristics have been assumed for the parallel resistance model, based on [29,52–54].

A proper term for the surface transport should be identified. Surface diffusion occurs as molecules move along a surface through continuous adsorption and desorption processes. Adsorption is particulary relevant at lower temperatures and/or high pressures. Generally, surface flow/diffusion can be described using three models [55].

1. Hydrodynamic model: The adsorbed gas is described as a liquid film that glides along the surface wall driven by a pressure gradient. Gilliland et al. used this approach to define their surface flow [56].
2. Hopping model: Molecules are assumed to hop from site to site along the surface through adsorption/desorption processes. The surface flux is then calculated using the mean hopping distance and the velocity that molecules have leaving the site. A detailed model to calculate the mean hopping distance was developed by Weaver and Metzner [57], while Ponzi et al. [58] developed a simpler way to estimate the mean hopping distance.
3. Random walk model: This model has been developed based on the two-dimensional form of Fick's law, and used by Ash, Barrer and Pope [59] and Okazaki et al. [60].

Random walk models are generally better suited for heterogeneous surfaces found on carbon surfaces [61–64]. However, they are more complex, adding to the amount of fitting parameters. We therefore implement the hydrodynamic model to describe surface diffusion as reported by Gilliland et al. [56], chosen for its simplicity. As this is the only type of surface transport considered for carbon membranes in the

Table 1 – Integration parameters for normal distribution expression in equation (12).

k	a_k	b_k	Mechanism
0	0	1	–
1	1	$\bar{r}$	Surface flow
2	$\bar{r}+r$	$\bar{r}^2+r^2$	Molecular sieving
3	$\bar{r}^2+\bar{r}r+2\sigma_N^2+r^2$	$\bar{r}^3+3\bar{r}\sigma_N^2$	Slip flow, Knudsen diffusion
4	$\bar{r}^3+\bar{r}^2r+5\bar{r}\sigma_{N^2+\bar{r}}r^2+3\sigma_N^2r+r^3$	$\bar{r}^4+6\bar{r}^2\sigma_N^2+3\sigma_N^4$	Viscous flow

Table 2 – Transition points between mass transport phenomena as found in literature (r_p in nm).

Viscous flow	Slip/Transition flow	Knudsen diffusion	Surface diffusion	Molecular sieving
$3\lambda < r_p < r_{max}$	$\max(1,0.05\lambda) < r_p < 3\lambda$	$1 < r_p < \max(1,0.05\lambda)$	$0.3 < r_p < r_{max}$	$r_p < 0.3$

model, the total surface transport per chemical species j is written as

$$J^{s}_{tot,j} = \frac{RT\rho^{app}_{mem}}{\tau^2 C_{R,j} S_s \delta^{act}_{mem}} \int_{p_{perm,j}}^{p_{ret,j}} \frac{q_j^2}{p} dp \tag{13}$$

where q is the adsorbed amount of gas per weight of membrane, described by an isotherm model. The specific surface S_s of the membrane structure is defined as the total surface area inside the membrane over which adsorbed species are mobile per weight of the membrane. The total specific surface area is calculated by multiplying the internal area of a single perfectly cylindrical capillary ($2\pi r_p l_p$) with a shape-weight factor C_{sw}. This factor accounts for the porous network, which deviates from a bundle of perfectly cylindrical pores, as well as the weight of a single pore.

$$S_s = 2\pi r_p l_p C_{sw} \tag{14}$$

After applying the pore size distribution from eq. (1) and assuming that the length of the capillary l_p is equal to the thickness of the active membrane layer δ^{act}_{mem}, the expression becomes

$$S_s = \sqrt{2\pi}\, \frac{n_p}{\sigma_N} \delta^{act}_{mem} C_{sw} \int_{r^{low}_{su}}^{r^{high}_{su}} Q_1(r) dr \tag{15}$$

The final surface transport flux becomes

$$J^{s}_{tot,j} = \frac{RT\rho^{app}_{mem}}{\tau^2 C_{R,j} C_{sw} (\delta^{act}_{mem})^2 \sqrt{2\pi}\, \frac{n_p}{\sigma_N}} \frac{\int_{p_{perm,j}}^{p_{ret,j}} \frac{q_j^2}{p} dp}{\int_0^{r_{max}} Q_1(r) dr} \tag{16}$$

where q is computed via a Langmuir model:

$$q_j = q_{m,j} \frac{C_{L,j} p_j}{1 + C_{L,j} p_j} \tag{17}$$

The Langmuir coefficient can be defined with an Arrhenius equation:

$$C_{L,j} = C^0_{L,j} \cdot \exp\left(- \frac{\Delta H_{ads,j}}{RT} \right) \tag{18}$$

The isotherm integral inside eq. (16) can therefore be solved algebraically as

$$\int_{p_{perm}}^{p_{ret}} \frac{q_m^2}{p} \left(\frac{C_L p}{1 + C_L p} \right)^2 dp = q_m^2 \left(\frac{1}{C_L p_{ret} + 1} - \frac{1}{C_L p_{perm} + 1} + \ln\left(\frac{C_L p_{ret} + 1}{C_L p_{perm} + 1} \right) \right) \tag{19}$$

The resulting equation for the surface flux is

$$J^{s}_{tot,j} = \frac{RT\rho^{app}_{mem}}{\tau^2 C_{R,j} C_{sw} (\delta^{act}_{mem})^2 \sqrt{2\pi}\, \frac{n_p}{\sigma_N}} \frac{q_m^2 \left(\frac{1}{C_L p_{ret}+1} - \frac{1}{C_L p_{perm}+1} + \ln\left(\frac{C_L p_{ret}+1}{C_L p_{perm}+1} \right) \right)}{\int_0^{r_{max}} Q_1(r) dr} \tag{20}$$

2.2. Role of water and pore blocking factor

The presence of water in the membrane pores can severely impact gas separation performance in CMSMs. Water can produce functional groups containing oxygen and additionally adsorb on the pore surface, effectively reducing the pore size and inducing hydrophilicity, as shown by Llosa et al. [42]. They reported an increase in O_2/N_2 permselectivity with a reduced permeance due to oxygen chemisorption and water physical adsorption. While water strongly affects mass transport in carbon membranes, the adsorption and condensation of water inside the pores is a reversible process. During the membrane synthesis, water is removed by increasing temperature, a process referred to as membrane activation [3]. The membrane is exposed to an inert atmosphere (such as N_2 or He) at elevated temperatures for a period of time, effectively desorbing the water. The rate of desorption will depend on the interaction of the water molecules with the functional groups on the wall as well as the operating conditions. Membranes carbonized at intermediate temperatures will have more functional groups on the walls, potentially resulting in more water adsorption. Carbonization at higher temperatures will remove more functional groups, reducing the interaction strength of the water molecules with the pore walls. The required membrane activation temperature will therefore be lower. Not surprisingly, the exposure to higher temperatures can lead to a shift in dominant transport mechanism due to the change in effective pore size as water adsorbs or desorbs. A similar activation effect can be achieved by introducing high pressures inside the membrane, effectively pushing out water molecules. An increasingly high pressure would need to be applied to achieve any activation as pore sizes decrease.

Different approaches exist in literature that describe capillary condensation inside membrane pores. Hwang and Lee [65] proposed a model with six flow modes depending on the degree of capillary condensation. This model has also been applied to CMSMs by Poto et al. [66]. The six flow model, however, is only valid when water molecules can be assumed to be in a continuum regime, meaning that an actual condensed state is present in the pores. Generally for CMSMs, whose very small pore sizes approach the size of the permeating molecules, water present in the pores cannot be assumed to be in continuum regime. The size of the pores only facilitates singular water molecules in a very restricted nanoconfined passage, in an activated diffusion regime. Phase transitions such as capillary condensation are greatly affected by system dimensions and surface interactions [67]. Critical capillarity effects involve reversible and irreversible filling of pores based on the dimensions, critical pressure and critical temperature of the system [68]. Classical hydrodynamics do not hold inside nanopores where a continuum fluid regime cannot take place. In light of the complexity of the system, which calls for nanoscale description, and the scope of our model, which is meant for reactor-scale modelling, we propose here to describe water pore blocking with a simple pore blocking factor f_{pb}. This factor is defined as

$$f_{pb}(p, T) = \tanh\left(C_{pb,a} \cdot T^{C_{pb,b}} p^{C_{pb,c}} \right) \tag{21}$$

This factor varies between 0 and 1, where $f_{pb} = 0$ results in full pore blocking for low temperature and pressure, and $f_{pb} = 1$ means all the pores are opened up and no pore blocking occurs at high temperature and pressure.

$$\lim_{p,T\to 0}(f_{pb}) = 0 \tag{22a}$$

$$\lim_{p,T\to \infty}(f_{pb}) = 1 \tag{22b}$$

The resulting pore blocking becomes negligible at high temperature and pressure: For temperatures and pressures above the membrane activation, the pore blocking factor can be approximated to be 1. The pore blocking factor is then implemented in the mass transport model described above. We do this by considering two different expressions, one for gaseous transport and one for surface transport. Gaseous transport is limited as water molecules add an additional barrier of diffusion through the pore voids. Therefore, the pore blocking factor can be used to describe the shrinkage of the pore size due to water molecules attaching to the pore walls. Assuming the shape of the pore size distribution does not change as a result of this shift caused by pore blocking, the pore blocking factor multiplies the mean pore radius ($\bar{r}_p$).

$$\bar{r}_{p,pb} = \bar{r}_p \cdot f_{pb} \tag{23}$$

$\bar{r}_{p,pb}$ is the (apparent) mean pore radius for all gaseous transport mechanisms affected by pore blocking. Surface diffusion is instead limited because of the competition for adsorption on the active sites of the pore walls between the permeating gas species and the water molecules. Accordingly, the pore blocking factor for surface diffusion is implemented by multiplying the maximum adsorbed amount for a monolayer with the pore blocking factor, thus reducing the available active sites due to water.

$$q_{m,pb} = q_m \cdot f_{pb} \tag{24}$$

2.3. *Parameter estimation*

The model presented above was then applied to describe permeation through different membranes and different gases (pure and multi-component mixtures). The experimental setup and permeation tests are described in the next section. As key part of the model application, unknown parameters must be estimated from experimental results. The parameter estimation is formulated as a problem of minimization of the sum of squared residuals (SSR), where the flux is used as a target variable:

$$SSR = \sum_{i=0}^{n}\left(J_{exp,i} - J_{num,i}\right)^2 \tag{25}$$

In order to quantify the quality of a fit, the R-squared is used:

$$R^2 = 1 - \frac{\sum_{i=0}^{n}\left(J_{exp,i} - J_{num,i}\right)^2}{\sum_{i=0}^{n}\left(J_{exp,i} - \overline{J_{exp}}\right)^2} = 1 - \frac{SSR}{SST} \tag{26}$$

The model has a rather large number of fitting parameters (listed in Table 3). Not surprisingly, the resolution of the fitting problem is numerically complex. Therefore, multiple global optimization algorithms were tested and compared, namely Particle Swarm, Genetic Algorithm and Global Search in the Global Optimization Toolbox in MATLAB. Particle Swarm and Genetic Algorithm showed promising results and lower initial guess dependency compared to Global Search. Particle Swarm Optimization (PSO) proved to be the most efficient for fitting and it was chosen due to its ability to handle high number of fitting parameters and degree of freedom. PSO is a stochastic population-based algorithm where individual particles move step-wise through a region where the algorithm evaluates the objective function at each particle step.

Table 3 – Fitting parameters and boundary conditions for the parallel resistance model.

Parameter	Unit	Lower boundary	Upper boundary
$\bar{r}_p$	[m]	r_{kin}^{min}	1e-6
$C_R \cdot C_{sw}$	[(m^2 ·s)]	0	∞
C_L^0	[–]	0	∞
C_{ms}	[mol /m ·s ·Pa]	0	∞
ΔH_{ads}	[J /mol]	-1e6	0
$E_{act,ms}$	[J /mol]	0	1e6
σ_N	[m]	0	1e-6
$n_p\left(\sim \frac{A_m e m \epsilon}{\pi \bar{r}_p^2}\right)$	[–]	1e11	5e16
q_m	[mol /kg]	0	7
τ	[–]	1	100
$C_{pb,\{a,b,c\}}$	[–]	0	∞

A key step in parameter fitting is the choice of physically sound boundary conditions. Table 3 gives an overview of the fitting parameters with the chosen fitting boundaries. Both the mean pore radius ($\bar{r}_p$) and the standard deviation (σ_N) are dependent on the pore size distribution. As the focus of this work is CMSMs for gas separation, the upper bound for both was set to be 1 μm. The lower bound for the mean pore radius was set to the kinetic (or collisional) radius of the smallest permeating gas. The adsorption enthalpy (ΔH_{ads}) was assumed negative (exothermic) with a lower limit of −1000 kJ/mol (−239 kcal/mol). Typical energy ranges are 2–10 kcal/mol for physisorption and 15–100 kcal/mol for chemisorption [61]. Molecular sieving is an activated process which has a positive activation energy ($E_{act,ms}$). The minimum was set to 0 and the maximum to 1000 kJ/mol. The total number of pores has been estimated using eq. (4), where the lower bound and upper bound are estimated using expected ranges for membrane porosity (ϵ) and mean pore radius in the tested CMSMs. The upper bound for the adsorbed amount at full monolayer coverage (q_m) for all gasses (H_2, N_2, CO_2) has been chosen based on adsorption data on activated carbon from various works between 0 and 30 °C and 7–10 bara. These ranges are consistent with the conditions used for CMSM tests in this work. The maximum capacity found was 0.275–0.5 mol/kg for H_2 [69,70], between 1 and 1.4 mol/kg for N_2 [69,71], and 4.3–7 mol/kg for CO_2 [71,72]. The upper bound for q_m was therefore set to 7 mol/kg. The tortuosity of the membrane pores (τ) will always be equal to or larger than 1. As for the remaining mass transport related coefficients (C_R, C_{sw}, C_L^0, C_{ms}, $C_{pb,\{a,b,c\}}$), no suitable physical boundaries could be determined other than the assumption they are non-negative.

3. Experimental setup and tests

Four tubular CMSMs were synthesized and tested. The synthesized membranes are named M1 - M4 and an overview of the characteristics is reported in Table 4. M1 is a highly H_2/N_2 selective carbon membrane derived from hydroquinone, with a 2-layer structure fabricated on a zirconia support with an average pore size of 120 nm. M2 is fabricated from a Novolac precursor supported on α-alumina containing a top layer with an average pore size of 100 nm. M3 and M4 differ from M2 in the molecular weight of the precursor used for the synthesis. Membranes were tested for pure/single gas conditions, while only M4 was used for testing multi-component mixtures.

The thickness in Table 4 refers to active membrane thickness.

3.1. Membrane synthesis

In the following section, we describe the membrane synthesis in more detail for the Novolac membranes (M2-M4). The synthesis of M1 is similar where phenol is replaced by hydroquinone as a reactant. Oxalic acid (98%), formaldehyde (37% VWR chemicals), N-methyl-2-pyrrolidone (NMP, 99.5%), and phenol for synthesis were supplied by Merck. Asymmetric tubular porous alumina and zirconia supports were supplied by Inopore GmbH with outer diameters (OD) of 10 mm (M1, M2 and M4), 14 mm (M3), and inner diameters (ID) of 7 mm. The external layer of alpha alumina and zirconia has an average pore size of 100 nm. Porous supports were connected to a dense alumina tube via glass sealings prepared at 950 °C with 10 min curing time. The supported membranes were prepared by dipping the porous support into a solution containing Novolac oligomer precursor, NMP, oxalic acid and formaldehyde. The quantity of the materials, used equipment, and the detailed procedure at each step of the synthesis were as follows.

3.2. Precursor synthesis and dipping solution preparation

Novolac synthesis in this work has followed the synthesis procedure reported in our previous work [73]. Firstly, 23 g (0.24 mol) of phenol was melted at 50 °C in a four neck round bottom glass flask which was equipped with a reflux condenser. Then, 0.5 g of oxalic acid was added to the solution, and the temperature was increased to 85 °C, while 14 g (0.17 mol) of formaldehyde solution was added to the solution in a drops. The reaction was continued for 5 h, the solution was centrifuged at 10 °C, and was rinsed with deionized water 3 times with a speed of 4400 rpm for 20 min in each step. Finally, the oligomer was collected in a porcelain dish and was vacuum dried at 50 °C for 24 h 30 g of the resulted oligomer was dissolved in 83 g of NMP in a high shear mixer (Thinky ARE-250) with 2000 rpm speed for a duration of 30 min. Then, 0.1 g of oxalic acid was added to the solution and mixed for 30 min in 1500 rpm. In the next step, 1.2 g of formaldehyde solution was added to the solution and mixed for two cycles of 20 min at 1600 rpm.

3.3. Dip coating, polymerization, and carbonization

The prepared alumina supports were dip coated in an automatic dipping machine with upper speed and lower speed of respectively 5 mm/s and 10 mm/s and 10 cycles of dipping. Then, the coated supports were moved to a rotary oven and polymerized under a nitrogen atmosphere for 24 h at 60 °C at continuous rotation of 30 rpm. Next, the membranes were transported to a 3-zone tubular oven (Nabertherm R 170/1000/1) and carbonized under an argon or nitrogen atmosphere with a final carbonization temperature of 500 and 600 °C. The second layer of carbonization was repeated as explained before and only conditions such as the dip coating parameters were fine-tuned for each membrane. Finally, the CMSMs were post-treated in a humidification chamber with 100% relative humidity (RH) at room temperature for one week for saturation of the hydrophilic sites and stabilization of the membrane.

3.4. Membrane permeation tests

After fabrication and aging, the CMSMs (M1, M2, M3) were installed in a setup for gas permeation tests. The setup contains four main parts including the gas feeding, a (reactor) vessel with membrane, the permeate flow measurements, and controlling elements, i.e. back pressure controller. Each membrane was installed in the reactor and dried by a N_2 stream at a 2 bar pressure difference between the retentate and permeate for 24 h. This pre-treatment is required to remove the condensed water in the pores of the membrane and the support. All permeation tests were conducted at a feed rate of 5 NL/min. Fig. 3 provides a schematic of the permeation setup used for the tests.

After drying, the temperature of the membrane was set to the desired measurement temperature. After reaching the temperature, the targeted gas was injected, the pressure was set and a 30 min waiting time was applied for system stabilization. In the next step, the permeate flow rate was measured with a bubble flow meter (Horiba Stec) and an average flow rate over four separated measurements was recorded. Then, the next pressure was set and the four measurements were repeated. This process was continued from highest to lowest pressure. Next, the pressure was released, N_2 was temporarily injected for flushing, and the next gas was injected as

Table 4 – Membrane characteristics.

Name	Type	Precursor	Support	Length	Thickness	Gas tests	Carbonization T
M1	CMSM	Hydroquinone	Zr	340 mm	6.7 μm	Pure	600 °C
M2	CMSM	Novolac	Al-100	100 mm	7 μm	Pure	500 °C
M3	CMSM	Novolac	Al-100	88 mm	7 μm	Pure	500 °C
M4	CMSM	Novolac	Al-100	190 mm	8.6 μm	Pure & Mixed	500 °C

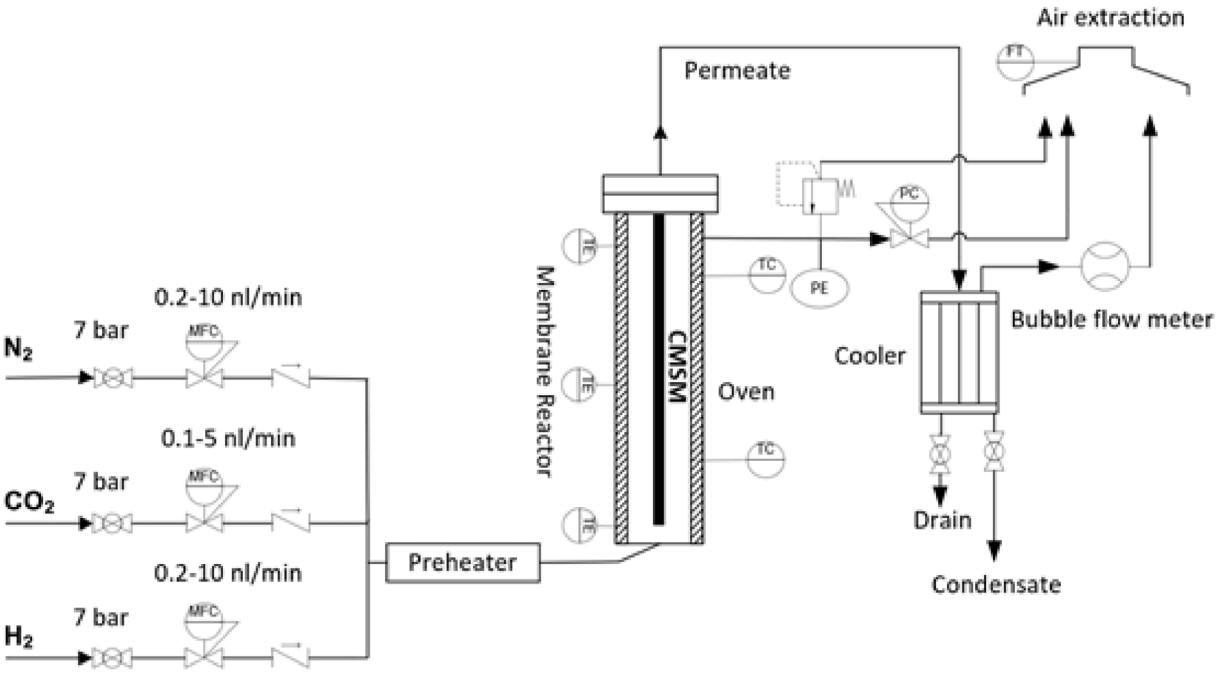

Fig. 3 – Schematic representation of membrane reactor for gas permeation tests.

described before. This process was repeated for all the single gas tests (CO_2, N_2 and H_2). After this procedure, the next temperature was set and N_2 flushing continued until the set temperature was reached. The measurements were repeated for all temperatures and backward measurements were carried out to validate the reproducibility. Experimental deviation from the average flow rate was below 3% for all points. For the multi-component permeation gas tests of M4, a similar setup and procedure was used with the only difference being the addition of a vacuum pump on the permeate side to increase driving force. The outlet permeate composition was subsequently measured with a gas chromatograph (Agilent 490μ GC).

For membranes M1, M2, M3 investigated in this work, the ideal H_2/N_2 selectivities are reported in Table 5. These ideal selectivities have been calculated according to the ratio of the permeances. Permeation of these CMSMs were tested for pure components (H_2, N_2 and CO_2) as a function of temperature (T 45–470 °C) and pressure (Δp 1–6 bar). The full overview of permeation data can be found in the Supplementary Data inside the Appendix. It can be seen that M1 shows high H_2/N_2 permselectivity at 150 °C and 2 barg. This indicates that molecular sieving effects are dominant. M1 has in fact very small pores as hydroquinone is chosen as a polymerization precursor. M2 shows ideal Knudsen permselectivity for temperatures higher than 50 °C, indicating Knudsen diffusion is the dominating mechanism. The H_2/N_2 permselectivity is slightly higher for lower temperatures, suggesting pore blocking effects. The H_2/N_2 permselectivity of M3 is higher than ideal Knudsen permselectivity, but lower than M1, which suggests mixed behaviour. M3 has a higher degree of polymerization, resulting in a better porous

Table 5 – Measured ideal H_2/N_2 gas-pair permselectivity data for membranes M1-M3.

M1 H_2/N_2 selectivity	45 °C	75 °C	100 °C	150 °C	200 °C	260 °C	350 °C	470 °C
Δp 1 bar	90.5	122.3	124.6	295.1	184.0	40.5	31.4	46.2
Δp 2 bar	79.2	106.6	139.0	302.1	171.7	42.1	34.3	45.7
Δp 4 bar	63.8	79.2	121.9	254.0	159.1	43.3	33.0	47.7
Δp 6 bar	48.9	71.3	109.4	229.8	161.6	43.6	33.6	47.1
M2 H_2/N_2 selectivity	20 °C	50 °C	100 °C	150 °C	200 °C			
Δp 1 bar	12.7	7.0	3.7	4.1	4.0			
Δp 2 bar	10.3	6.6	3.8	3.6	4.0			
Δp 4 bar	8.3	6.2	3.7	3.7	4.0			
Δp 6 bar	5.7	5.4	3.2	2.7	3.5			
M3 H_2/N_2 selectivity	20 °C	50 °C	100 °C	150 °C	200 °C			
Δp 1 bar	4.4	21.0	13.2	9.3	12.4			
Δp 2 bar	3.7	15.4	12.2	11.0	9.2			
Δp 4 bar	3.5	18.2	12.0	10.6	8.8			
Δp 6 bar	3.5	15.7	10.6	10.4	8.5			

network after carbonization. This results in a better H_2/N_2 permselectivity.

4. Results and discussion

4.1. Single gas results (M1, M2, M3)

The parallel resistance model is fit to permeation results reported in the Supplementary Data. For all pure gas fits, it can be assumed that the permeate side consists of the permeating gas exclusively. The permeate side pressure is assumed atmospheric as no vacuum pump or sweep gas is implemented and conditions inside the bubble flow meter are atmospheric. The fitting parameters for membranes M1-M3 and each gas are shown in Table 6. Note that ϵ is not a fitting parameter, but it is calculated based on the fitted values and equation (4). Two categories can be distinguished between the fitted parameters, namely membrane specific- and gas specific parameters. Membrane specific parameters are assumed constant irrespective of the permeating gas, as they are membrane properties. These are; $\bar{r}_p$, σ_N, n_p, τ. Gas specific parameters depend on properties of both the membrane and permeating gas. These are; C_R, C_L^0, C_{ms}, ΔH_{ads}, $E_{act,ms}$, q_m. The pore blocking parameters $C_{pb,j}$ will also depend on both the membrane- and gas properties. Different permeating gasses interact differently with water and other blocking contaminants, but these effects are generally minimal compared to other effects such as temperature and relative humidity. The apparent shrinkage of the pores and blocking of active sites should therefore not strongly depend on the permeating gas. However, this is not the case for membranes with very small pores, as these are strongly affected by molecular sieving effects and interactions. Therefore, the size difference between H_2 and N_2 becomes a key difference for the pore blocking factor the smaller the pores are. C_{pb} is therefore assumed a membrane specific parameter for all membranes except M1, where it is assumed to differ per gas. The permeation model is fit to all pure gases simultaneously, for each membrane respectively, as membrane specific parameters should not change per gas. The amount of fitting parameters is therefore $7 + 6*n_{comp}$ (nr. of membrane specific parameters + nr. of gas specific parameters * nr. of gasses). The results of the fitting are shown in Table 6. To investigate the robustness of the model, fitting has been repeated considering all fitting parameters for each gas and membrane separately. Results are reported in Table S3 in the Supplementary Material. All parameters (including membrane specific) have been given the freedom to reach different values per gas within the same membrane. Theoretically, all membrane specific parameters should respectively give the same value for different gasses. The results in Table S3 indeed show the membrane specific parameters to be overall consistent across the different permeating gasses with relatively small changes. This suggests that the model can identify the membrane properties consistently.

The results of the fitting for membranes M1-M3 are reported in Figs. 4, 5 and 7. The permeation of hydrogen in a highly H_2/N_2 selective hydroquinone membrane (M1, Fig. 4) has been experimentally determined with permeation tests for four different retentate to permeate side pressure drops (1 bar, 2 bar, 4 bar, 6 bar) for a temperature range of 45–470 °C and a permeate side pressure of 1 bara. The data of the 1, 2, and 6 bar curves has been used to fit the model, while the 4 bar data is used to evaluate the model predictive capabilities. The model is able to describe the experimental data and behaviour for this range of pressures and temperatures. Moreover, it can predicatively describe the permeation behaviour for operating conditions within the fitting boundary limits. It can be noted that hydrogen permeation is low at lower temperatures, but increases drastically as it approaches 100 °C. This is caused mostly by pore blocking due to water molecules. As the pores open up with increasing temperature, permeation increases. A drop in permeation between 100 and 150 °C can be seen for all four pressures. This is likely caused by decrease of surface diffusion with increasing temperature. Beyond 150 °C, permeation rises again as molecular sieving becomes dominant with increasing temperature. Overall the prevailing transport mechanisms inside this hydroquinone membrane are therefore surface diffusion and molecular sieving. This is further evidenced by the measured high ideal H_2/N_2

Table 6 – Model parameter values for different membranes and gasses. All parameters are fitting parameters except porosity (ϵ), which is calculated back using equation (4).

Membrane parameters		M1		M2		M3	
$\bar{r}_p$	[nm]	0.189		0.501		0.241	
σ_N	[nm]	0.210		0.199		0.272	
n_p	[–]	$1.00 \cdot 10^{1}5$		$1.01 \cdot 10^{1}5$		$1.09 \cdot 10^{1}4$	
τ	[–]	9.78		2.9		15.0	
$C_{pb,a}$	[–]	$1.04 \cdot 10^{-23}$	$4.89 \cdot 10^{-25}$	$1.72 \cdot 10^{-10}$		$1.92 \cdot 10^{-19}$	
$C_{pb,b}$	[–]	8.98	8.97	3.23		7.37	
$C_{pb,c}$	[–]	0	$3.96 \cdot 10^{-5}$	0.413		0	
ϵ	[–]	0.0105		0.254		0.0051	
Gas parameters		H_2	N_2	H_2	H_2	N_2	CO_2
$C_R \cdot C_{sw}$	$[1/(m^2 \cdot s)]$	138	166	$5.28 \cdot 10^{9}$	$4.16 \cdot 10^{1}0$	10.0	$9.00 \cdot 10^{7}$
C_L^0	[–]	$7.79 \cdot 10^{-14}$	$1.06 \cdot 10^{-14}$	$3.38 \cdot 10^{1}0$	$3.54 \cdot 10^{1}0$	$1.04 \cdot 10^{-11}$	$1.12 \cdot 10^{-9}$
C_{ms}	[mol/(m·s·Pa)]	$2.97 \cdot 10^{-10}$	$1.49 \cdot 10^{-11}$	$4.67 \cdot 10^{-17}$	$2.21 \cdot 10^{-11}$	$7.74 \cdot 10^{-12}$	$7.61 \cdot 10^{-12}$
ΔH_{ads}	[kJ/mol]	−60.0	−59.9	−60.1	0	−5.84	−35.0
$E_{act,ms}$	[kJ/mol]	9.94	12.6	10.6	3.30	8.21	3.93
q_m	[mol/kg]	$3.49 \cdot 10^{-5}$	$1.23 \cdot 10^{-4}$	$4.96 \cdot 10^{-5}$	0	$1.77 \cdot 10^{-3}$	$3.81 \cdot 10^{-3}$

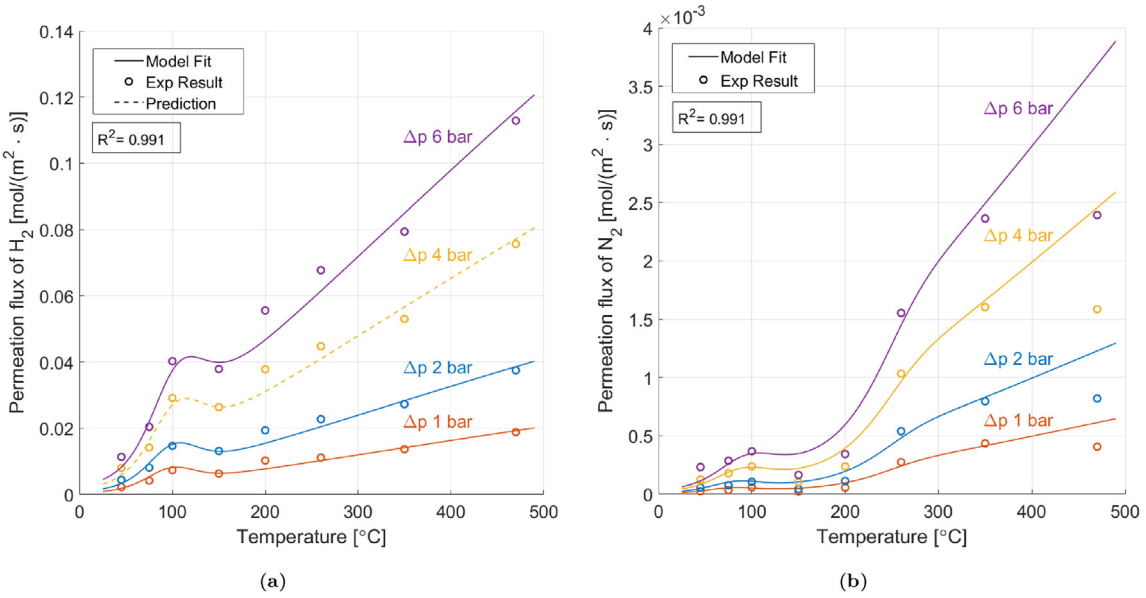

Fig. 4 – a). M1 membrane validation for pure H_2 permeation flux over temperature for several Δp. The 1, 2, and 6 bar curves are used for the model fitting, and the 4 bar curve is predictive. b). M1 membrane fit for pure N_2 permeation flux over temperature for several Δp.

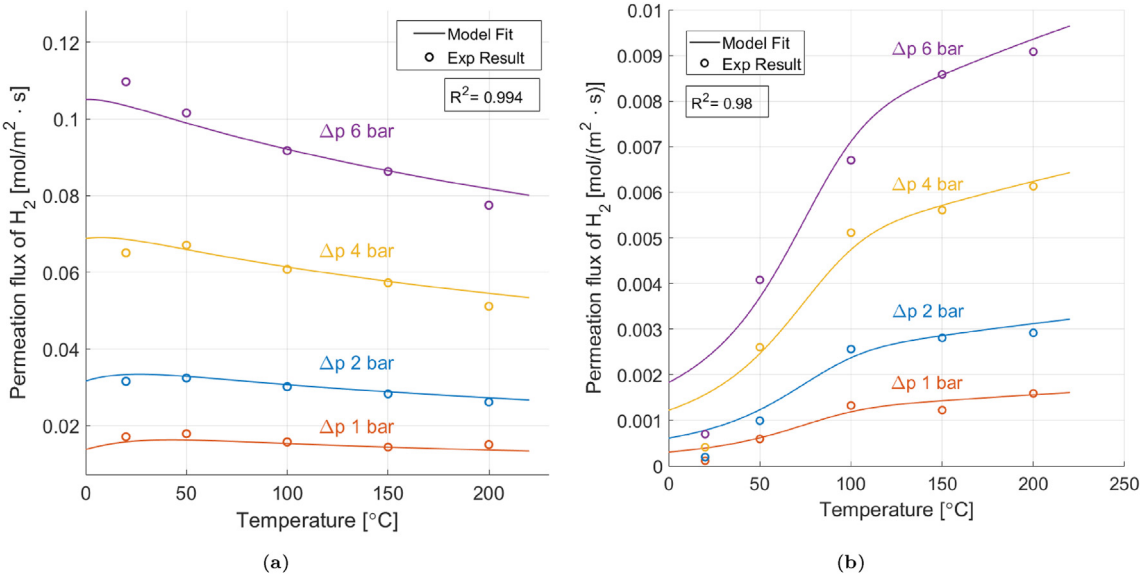

Fig. 5 – a). M2 membrane fit for pure H_2 permeation flux over temperature for several Δp b). M3 membrane fit for pure H_2 permeation flux over temperature for several Δp.

permselectivity shown in Table 5. The contribution of Knudsen diffusion is negligible as ideal Knudsen permselectivity for this gas pair lies around 3.73. Fig. 4b depicts the model and experimental results for permeation of nitrogen. The N_2 permeation curve is similar to the H_2 one. An initial increase is followed by a drop in permeation around 100–150 °C caused by surface diffusion, after which molecular sieving starts dominating at higher temperatures. It can be seen that the model does not predict N_2 permeation well at the highest temperature (470 °C). The experimental data consistently shows a plateauing effect at higher temperature, which cannot be described by the current model's continued rise in permeation due to molecular sieving. Possible causes for the plateauing of nitrogen permeation might be related to temperatures that approach the carbonization temperature of the membrane, where instability of the porous structure as well as reaction of the functional groups on the pore walls could start taking place. As the difference in size between pore diameter and nitrogen molecule diameter is minimal, these effects at high temperatures could strongly impact nitrogen permeation. Similar plateauing effects are expected for H_2 at an even higher temperature. However, this could not be validated with the current system due to membrane deterioration issues and limitations in the setup. Pore blocking mechanisms

in carbon membranes appear to be critical for low temperature operation. If no pore blocking occurred (e.g. above the membrane activation temperature), permeation increases roughly linearly with pressure ($J \propto \Delta p$). If this is the case for both H_2 and N_2 measurements, the ideal H_2/N_2 permselectivity should be constant irrespective of pressure. Looking at Table 5, this is true for temperatures above 200–250 °C. This no longer holds when pore blocking occurs. Below 200–250 °C, the permselectivity changes as a function of pressure as pore blocking affects both gasses differently. N_2 is larger and interacts differently with water. Looking at the dependency between permeation flows and pressures in Table S1 in the Supplementary Material, the membrane activation temperature appears to lie between 100 and 150 °C for H_2 and between 200 and 250 °C for N_2 for M1.

The permeation of H_2 through membranes M2 and M3 has been measured for four pressure drops in a temperature range (20–200 °C). The parallel resistance model was fit to this data and results are shown in Fig. 5a and b. Both fits show relatively good accuracy. Membrane M2 (Fig. 5a) shows a decrease in H_2 permeation with increasing temperature, which suggests the membrane is dominated by Knudsen diffusion. Table 5 confirms this prediction, showing almost ideal Knudsen permselectivity close to 3.73 at temperatures higher than 50 °C. Not surprisingly, M2 has significantly larger pores ($\bar{r}_p = 0.501$ nm) as predicted by the fitting and confirmed by experimental synthesis features. It can be seen at 20 °C that there is a slight decrease in permeation flux for a driving force of 1, 2, and 4 bar. This is likely caused by pore blocking. As the driving force goes from 4 bar to 6 bar, this flux at 20 °C increases rapidly. At sufficiently high pressures, the permeating gas molecules likely push out adsorbed water molecules that block the pores which leads to an increase in permeation flux. The model is not able to accurately describe this phenomenon as the shape of the hyperbolic tangent representing the pore blocking factor is not able to accurately mimic this behaviour. The H_2/N_2 permselectivity for M2 in Table 5 supports these claims. The model also fits H_2 permeation in membrane M3 rather well, as shown in Fig. 5b. Model and experimental results show that H_2 permeation rapidly increases at temperatures below 100 °C, especially at high pressure difference. This initial rapid increase also suggests pore blocking effects in line with M1 and M2. The model overpredicts H_2 permeation at 20 °C especially for higher pressures, possibly because of the simplicity of the pore blocking model. The overall H_2/N_2 permselectivity of M3 is higher than ideal Knudsen permselectivity even at high temperatures, suggesting a mix of transport mechanisms and the presence of molecular sieving.

In order to have a better representation of the contribution from the different transport mechanisms, we show the separate weighted contributions in Fig. 6. The curves in the individual mechanisms are independent from each other and cumulatively add up to the total flux depicted with a solid line. We do this for the H_2 permeation flux of membranes M1, M2, and M3 at 6 bar. For M1, the model predicts a combination of molecular sieving and surface diffusion to be dominant at low temperatures. Pore blocking decreases with increasing temperature until 100 °C, after which surface diffusion starts dropping and molecular sieving dominates. These findings are in line with previous observations based on experimental permselectivities in Table 5. For M2, the model predicts Knudsen diffusion to be the only relevant transport mechanism. This is in line with experimental permselectivity, which is very close to ideal Knudsen permselectivity. For M3, the model shows predominantly molecular sieving, with strong pore blocking effects at lower temperatures. Viscous flow and slip flow are mostly irrelevant for these three membranes as the pores are too small for these transport mechanisms.

Fig. 7 depicts the results of N_2 and CO_2 pure gas permeation for membrane M3. The experimental N_2 curve has a shape similar to the M3 H_2 curve shown in Fig. 5b. The sharp increase in permeation flux at low temperatures suggests that pore blocking is prevalent for both N_2 and CO_2. The experimental CO_2 curve deviates from the H_2 and H_2 curves at temperatures above 100 °C, where the permeation flux appears to achieve a maximum and even decrease. This is likely related to a decrease in surface diffusion at higher temperature, as surface diffusion is expected to be predominant for CO_2 permeation; polar molecules such as CO_2 have slightly stronger surface interactions than non-polar and very weakly adsorbable gases such as H_2 and N_2. Moreover, CO_2 permeation at 100 °C increases as a function of pressure. This is also consistent with a higher adsorption capacity at higher pressures. Overall, the model is capable of following these trends with reasonable accuracy.

Fig. 8 shows the separate contributions of the transport mechanisms for N_2 and CO_2 in M3 at a pressure difference of 6 bar as predicted by the model. N_2 permeation appears to be predominantly determined by molecular sieving similarly to the H_2 curve, while a small contribution of Knudsen diffusion and slip flow are predicted. It is surprising to find both slip flow and molecular sieving present without any Knudsen diffusion for lower temperatures. Additionally, the shape of the slip flow curve shows a sharp bend around 75 °C after which Knudsen diffusion appears. This is caused by the chosen boundaries of the transition radii between the mass transport phenomena shown in Table 2. A combination of constant values and values dependent on the mean free path have been assumed for these transition radii. In reality, these values should slightly differ depending on the specific characteristic of the functional groups and characteristics of the membrane and system. These assumptions therefore result in the curves seen in the figure. The CO_2 permeation curve shows that the model predicts a combination of molecular sieving and surface diffusion. This is in line with expectations described above.

It is worth stressing that attention has to be paid when interpreting model results. The higher the degrees of freedom in the model, the more probable the model fits a curve accurately while failing to capture the physical relevance of the system and its behaviour. Realistic boundary conditions and physically sound assumptions are therefore crucial. Furthermore, the model is still dependent on a reasonable initial guess despite the global optimization scheme.

Finally, we can compare the three membranes based on the values of their fitting parameters shown in Table 6. The average fitted pore size increases as M1 < M3 > M2. This is in line with ideal selectivities as M1 has the highest permselectivity followed by M3, both of which show molecular

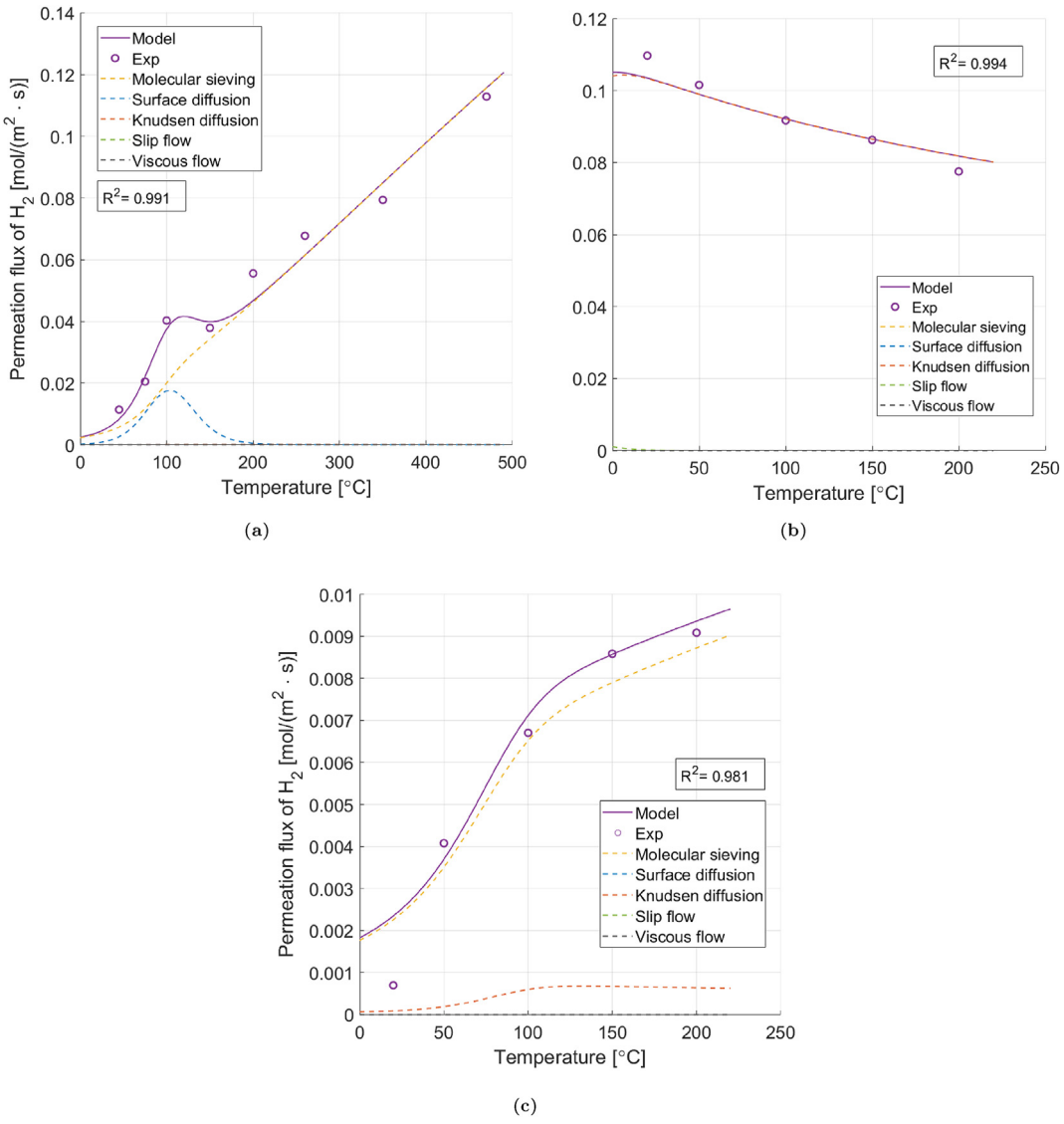

Fig. 6 – Separate contributions of each transport mechanism for pure H_2 permeation flux at Δp 6 bar in membrane a.) M1 b.) M2 c.) M3.

sieving effects. M2 has the largest fitted pore size, which is also expected given that it is dominated by Knudsen diffusion. When comparing the adsorption energy and surface coverage for H_2, N_2, and CO_2 of M3, it can be seen that CO_2 is predicted to have the highest (exothermic) adsorption energy and the highest monolayer coverage, meaning that adsorption will be strongest. This is also in line with physical intuition. However, when looking at the values of $C_R \cdot C_{sw}$, C_L^0 and C_{ms}, it can be seen that values can vary wildly from orders of magnitude equal to 10^{-17} up until 10^{10} with little physical relevance. This is a critical point for all models with fitting parameters. These wide ranges are inherent to the form of the chosen equations. For surface diffusion, C_R is implicit to the chosen hydrodynamic model. Furthermore, C_L^0 is implicit to the selected adsorption isotherm. C_{ms} stems from the simplified form in which molecular sieving was described. Despite these limitations, our work provides a global fitting procedure allowing for more realistic physical limits.

4.2. *Multi-component mixture results (M4)*

Permeation tests for M4 consisted of both pure gas- and mixed gas measurements. Similar to M1-M3, pure H_2, N_2, and CO_2 permeation was measured as a function of temperature (T 50–300 °C) and pressure (Δp 1–6 bar). Subsequently, mixed permeation tests were carried out with a composition of 4 mol % H_2, 85 mol% N_2, and 11 mol% CO_2. The permeation results can be found in the Supplementary Material (Table S2). The multi-component system contains a vacuum pump operating at 15 mbar. The permeate side composition was measured with a gas chromatograph for the experimental points, while it is unknown for the modelling points in between. To circumvent this issue, the model was restructured for multi-component fits with the permeate partial pressures expressed as

$$p_{perm,i} = p_{perm}\frac{J_i}{J_{tot}} \tag{27}$$

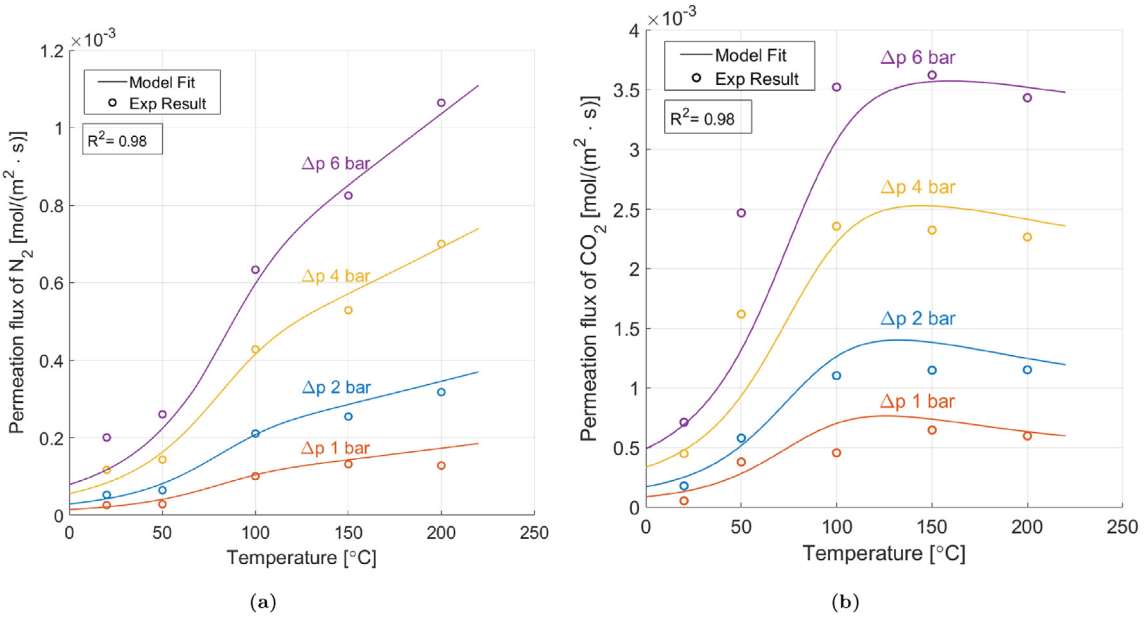

Fig. 7 – a). M3 membrane fit for pure N_2 permeation flux over temperature for several Δp b). M3 membrane fit for pure CO_2 permeation flux over temperature for several Δp.

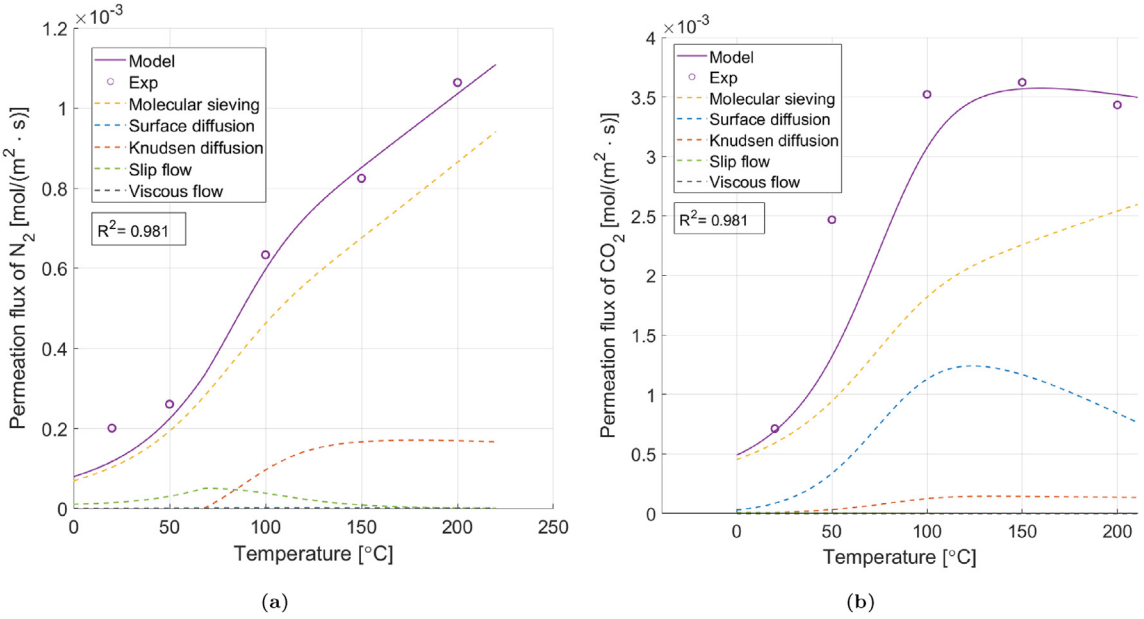

Fig. 8 – a). Separate contributions of each transport mechanism for pure N_2 permeation flux in membrane M3 at Δp 6 bar. b). Separate contributions of each transport mechanism for pure CO_2 permeation flux in membrane M3 at Δp 6 bar.

The total permeate pressure is 15 mbar, and the total permeation flux is a sum of the partial fluxes [$J_{tot} = \sum_i (J_i)$]. An iterative procedure is therefore required as the partial pressures necessary to calculate the flux are a function of the flux itself (J_{tot}). This was solved with an internal loop, minimizing the difference between this flux and the function of itself. We used fsolve in MATLAB.

The results of the multi-component mixture fit are shown in Fig. 9. Fig. 9a shows the parity plot of fitting parameters excluding the points used for validation, while Fig. 9b shows the validation curves for a pressure drop of 3.985 bar for the permeating gasses. The model shows relatively good agreement with the experimental data. As for Fig. 9a, most points are within a 95% confidence interval. The model correctly reproduces the trends for the different gases, as shown in Fig. 9b.

Model fitting was also done on pure gas measurements for M4, which can be found in Fig. S1 in the Supplementary Material. The permeation flux of H_2, N_2, and CO_2 can be seen as a function of temperature for several pressures. The model predicts the overall trends, however the low temperature behaviour for N_2 and CO_2 is not well represented

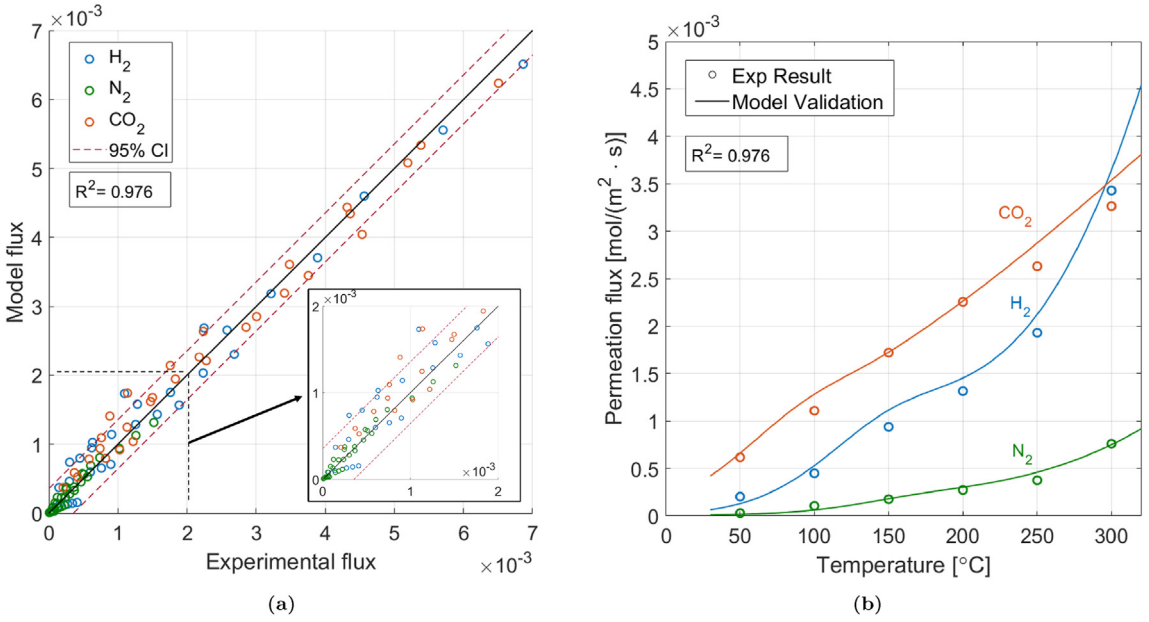

Fig. 9 – a). M4 parity plot for all mixed gas fitting points, excluding the points used for validation. The mixture contains 4 mol% H_2, 85 mol% N_2, and 11 mol% CO_2 for all points. b). M4 membrane model validation curves at $\Delta p = 3.985$ bar.

quantitatively. This is likely due to the simplicity of the pore blocking model. The pore blocking parameters $C_{pb,i}$ are assumed membrane parameters, meaning they are the same irrespective of the gas. The individual interaction of the permeating gases with the partially blocked pores is likely not well represented by the simplified black-box approach. Secondly, the CO_2 curve overestimates permeation within a temperature range of around 100–200 °C. This is caused by the surface diffusion term described by the hydrodynamic model and Langmuir isotherm equation (Eq. 13–19). The model fails to accurately describe the change in slope as a function of the increasing pressure difference for this membrane. Complex heterogeneous structures such as the pore surface of carbon membranes call for a more detailed approach.

Comparing the pure gas curves (Fig. S1) and mixed gas curves (Fig. 9b), the flux of the pure gas measurements is considerably higher. Additionally, the permeation curve for pure CO_2 (Fig. S1c) shows a decrease at higher temperature, suggesting that surface transport is the dominating mass transport mechanism. This trend cannot be seen for the mixed gas CO_2 curve shown in Fig. 9b where permeation increases increasingly with temperature. These differences between the pure- and mixed gas curves strongly suggest multi-component effects that occur in the mixed gas measurements.

Table 7 shows the fitting parameter values for both pure gas and mixed gas fits of M4. It is worth noting that the membrane parameters are consistent when comparing the

Table 7 – Model parameter values for M4. All parameters are fitting parameters except porosity (ϵ), which is calculated back using equation (4).

Membrane parameters		M4 pure			M4 mixed		
$\bar{r}_p$	[nm]	0.221			0.222		
σ_N	[nm]	0.228			0.234		
n_p	[–]	$1.10 \cdot 10^{1}5$			$1.10 \cdot 10^{1}5$		
τ	[–]	6.53			6.51		
$C_{pb,a}$	[–]	$9.81 \cdot 10^{-16}$			$2.03 \cdot 10^{-16}$		
$C_{pb,b}$	[–]	5.68			5.82		
$C_{pb,c}$	[–]	0.0964			0.102		
ϵ	[–]	0.0283			0.0286		
Gas parameters		H_2	N_2	CO_2	H_2	N_2	CO_2
$C_R \cdot C_{sw}$	$[(m^2 \cdot s)^{-1}]$	$5.35 \cdot 10^{1}1$	$1.84 \cdot 10^{1}3$	$1.04 \cdot 10^{1}2$	$8.35 \cdot 10^{1}3$	$9.84 \cdot 10^{1}3$	$3.04 \cdot 10^{1}2$
C_L^0	[–]	$1.42 \cdot 10^{-10}$	$3.88 \cdot 10^{1}1$	$7.65 \cdot 10^{-10}$	$2.43 \cdot 10^{-9}$	$3.88 \cdot 10^{1}1$	$2.46 \cdot 10^{-10}$
C_{ms}	$[mol/(m \cdot s \cdot Pa)]$	$2.13 \cdot 10^{-8}$	$1.55 \cdot 10^{-10}$	$9.14 \cdot 10^{-9}$	$4.44 \cdot 10^{-8}$	$5.51 \cdot 10^{-10}$	$1.11 \cdot 10^{-10}$
ΔH_{ads}	[kJ/mol]	−43.9	−48.3	−38.9	−48.9	−48.2	−38.9
$E_{act,ms}$	[kJ/mol]	28.1	26.2	58.1	34.1	36.4	10.4
q_m	[mol/kg]	3.70	$1.29 \cdot 10^{-7}$	2.06	3.99	$1.20 \cdot 10^{-7}$	1.97

pure gas and mixed gas results. The pore size distribution, pore numbers, tortuosity, and porosity are found to be the same when fitting pure gasses or mixtures. On the other hand, the gas parameters show a greater deviation as multi-component effects influence the gaseous transport and surface diffusion. While multi-component effects are currently not considered in the parallel resistance model, the model is capable of describing the permeation for the mixture of interest. However we predict that the model would probably not be applicable for a significantly different mixture, which would require dedicated fitting.

The pore size distributions based on the fits for membranes M1-M4 are shown in Fig. 10. The predicted distributions for M1, M3, and M4 are close to each other as all of them show molecular sieving effects. M1 has the second smallest variance and smallest pore size, which is expected as it has the highest H_2/N_2 permselectivity. M2 has larger pores compared to all other membranes, which is not surprising given the dominant mechanism is Knudsen diffusion. M3 has the largest variance, which is supported by model predictions and experimental ideal H_2/N_2 permselectivity, both suggesting a mix of multiple transport mechanisms. The distributions of M4 for both the pure gas and multi-component mixture data is very close to each other. This is expected as membrane specific parameters should not depend on the gas mixture. Unfortunately, this model based pore size distribution could not be experimentally validated. Attempts to experimentally quantify the actual pore size distributions inside these membranes through BET and permporometry were as of yet unsuccessful due to the small pore sizes. However, the overall trends of the fit pore size distributions with respect to each other are in line with permselectivity results and the understanding of membrane properties based on the synthesis.

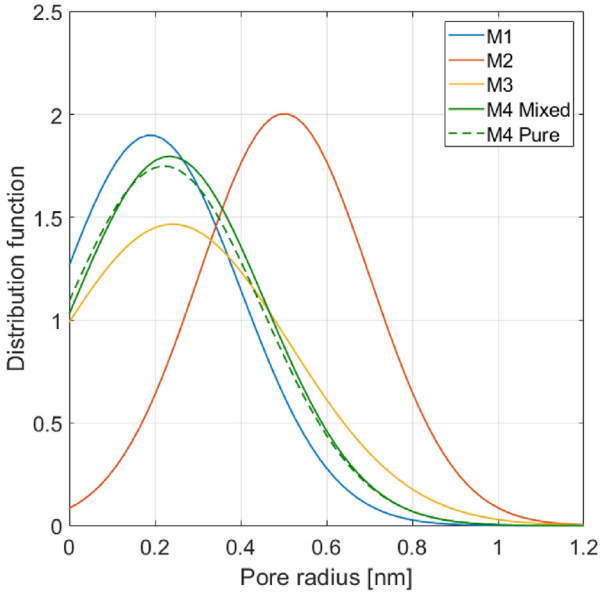

Fig. 10 – Fitted pore size distributions of membranes M1 - M4.

5. Conclusions

In this work, we provided a new mathematical model for computing gas permeation through carbon membranes. An experimental campaign was conducted using a permeation setup to measure pure and mixed gas permeation of several carbon membranes for a range of retentate pressures and temperatures. Building upon different literature approaches, a phenomenological model for pure gas permeation was developed for carbon membranes where parallel resistances and pore size distributions are implemented. The model was fit to the experimental permeation results using a Particle Swarm Optimization algorithm. The global fitting procedure outlined in this work allows for selection of realistic physical boundary conditions. As opposed to a simplified fitting methodology involving lumped fitting parameters, our procedure therefore facilitates a more in-depth and physically relevant analysis of model predictions.

The model was first fit to pure gas permeation measurements of three different carbon membranes. Experimental results showed that each membrane had different dominating transport mechanisms. The novel addition of a separate molecular sieving term as well as a black-box pore blocking term enabled our model to be able to describe the overall permeation for these membranes for a range of temperatures and pressures. Moreover, the model showed predictive capabilities within the operating boundaries of the fits. Splitting the permeation fluxes into their respective mass transport mechanisms, the model behaviour and experimental observations showed good agreement. H_2 and N_2 permeation in membrane M1 showed a combination of molecular sieving and surface diffusion at lower temperatures and mostly molecular sieving at higher temperatures. The activation temperature for pore blocking appears to be higher for N_2, possibly due to size difference and interaction with water. Additionally, a plateauing effect was observed for N_2 at high temperature. Possible causes for this are pore instability effects and changing interaction with surface functional groups which change with increasing temperature. H_2 permeation for membrane M2 displayed pure Knudsen diffusion, whereas membrane M3 showed mixed behaviour and strong pore blocking effects. CO_2 permeation was compared to H_2 and N_2 permeation in membrane M3. The model predicted surface diffusion to be more predominant for CO_2 permeation, in line with adsorption theory. When comparing the fitted values across membranes M1-M3, the predicted pore sizes and adsorption energies were in line with experimental expectations. The model was also fit to a fourth carbon membrane (M4), both for pure gas and mixed gas measurements. The model was able to predict the curves for both pure- and mixed gas measurements. However, the model does not account for multi-component effects so it will not be capable of reproducing different mixtures without prior fitting.

Several aspects are highlighted here, which should be improved regarding the model in future work. Firstly, multi-component effects should be accounted for as well as their influence on mass transport and surface interaction. Secondly, the current hydrodynamic film theory used for the surface transport term was chosen for its simplicity. Other

approaches such as hopping models and random walk models better suited for heterogeneous activated carbon structures should be investigated with the parallel resistance model. Thirdly, the pore blocking model should be improved to incorporate actual physical activation phenomena. To this end, molecular simulation can be used to research pore blocking and nano-confinement and aid the development of phenomenological pore blocking models. Furthermore, the pore size distribution of carbon membranes has been assumed to be a perfect Gaussian distribution, which is a critical assumption of the model. A real distribution will deviate to a certain degree from this ideal case, often with multiple peaks at different pore sizes. The effect of these non-ideal multi-modal distributions on the transport behaviour and its incorporation in the model should be investigated in more detail. Lastly, the boundaries for some of the considered fitting parameters could be further improved through experimental campaigns and molecular simulations. By linking these fitting parameters to synthesis parameters, the eventual aim would be to have a predictive model that can determine the permeation behaviour based on conditions such as precursor type and carbonization temperature without the need for fitting procedures. Production of carbon membranes could then be fine-tuned based on application and separation requirements per specific case using this model.

Declaration of competing interest

The authors declare that they have no known competing financial interests or personal relationships that could have appeared to influence the work reported in this paper.

Acknowledgements

INNOMEM has received funding from the European Union's Horizon 2020 Research and Innovation Program under Grant Agreement N° 862330.

Appendix A. Supplementary data

Supplementary data to this article can be found online at https://doi.org/10.1016/j.ijhydene.2023.08.272.

REFERENCES

[1] Sholl DS, Lively RP. Seven chemical separations to change the world. Nature Publishing Group, issn: 1476-4687 Nature Apr. 2016;532(7600):435–7. https://doi.org/10.1038/532435a [Online]. Available: https://www.nature.com/articles/532435a. visited on 04/20/2023.

[2] Moodley P, Trois C. 2 - lignocellulosic biorefineries: the path forward. isbn: 978-0-12-820297-5. In: Ray RC, editor. Sustainable biofuels, ser. Applied biotechnology reviews. Academic Press; Jan. 1, 2021. p. 21–42. https://doi.org/10.1016/B978-0-12-820297-5.00010-4 [Online]. Available: https://www.sciencedirect.com/science/article/pii/B9780128202975000104 (visited on 04/20/2023).

[3] Medrano JA, Llosa-Tanco MA, Pacheco-Tanaka DA, Gallucci F. Chapter 2 - transport mechanism and modeling of microporous carbon membranes. isbn: 978-0-12-816350-4. In: Basile A, Ghasemzadeh K, editors. Current trends and future developments on (bio-) membranes. Elsevier; Jan. 1, 2019. p. 39–58. https://doi.org/10.1016/B978-0-12-816350-4.00002-7 [Online]. Available: https://www.sciencedirect.com/science/article/pii/B9780128163504000027 (visited on 04/30/2021).

[4] Jang K-S, Kim H-J, Johnson JR, Kim W-g, Koros WJ, Jones CW, Nair S. Modified mesoporous silica gas separation membranes on polymeric hollow fibers. Publisher: American Chemical Society, issn: 0897-4756. doi: 10.1021/cm200939d. [Online]. Available Chem Mater Jun. 28, 2011;23(12):3025–8. https://doi.org/10.1021/cm200939d. visited on 10/17/2022.

[5] Lin H, Van Wagner E, Freeman BD, Toy LG, Gupta RP. Plasticization-enhanced hydrogen purification using polymeric membranes. Science Feb. 3, 2006;311(5761):639–42. Publisher: American Association for the Advancement of Science. doi: 10.1126/science.1118079. [Online]. Available: https://www.science.org/doi/10.1126/science.1118079 (visited on 10/17/2022).

[6] Bernardo P, Drioli E, Golemme G. Membrane gas separation: a review/state of the art. Ind Eng Chem Res May 20, 2009;48(10):4638–63. https://doi.org/10.1021/ie8019032. Publisher: American Chemical Society, issn: 0888-5885. (visited on 02/25/2021.

[7] Robeson LM. The upper bound revisited. issn: 0376-7388 J Membr Sci Jul. 15, 2008;320(1):390–400. https://doi.org/10.1016/j.memsci.2008.04.030 [Online]. Available: https://www.sciencedirect.com/science/article/pii/S0376738808003347 (visited on 11/29/2021).

[8] Fuertes AB, Centeno TA. Preparation of supported asymmetric carbon molecular sieve membranes. J Membr Sci Jun. 10, 1998;144(1):105–11. issn: 0376-7388. doi: 10.1016/S0376-7388(98)00037-4. [Online]. Available: https://www.sciencedirect.com/science/article/pii/S0376738898000374. visited on 04/29/2022.

[9] Ismail AF, Rana D, Matsuura T, Foley HC. Carbon-based membranes for separation processes. New York: Springer-Verlag; 2011. isbn: 978-0-387-78990-3. doi: 10.1007/978-0-387-78991-0. [Online]. Available: https://www.springer.com/gp/book/9780387789903. visited on 09/15/2021.

[10] Rungta M, Wenz GB, Zhang C, Xu L, Qiu W, Adams JS, Koros WJ. Carbon molecular sieve structure development and membrane performance relationships. Carbon May 1, 2017;115:237–48. issn: 0008-6223. doi: 10.1016/j.carbon.2017.01.015. [Online]. Available: https://www.sciencedirect.com/science/article/pii/S0008622317300258. visited on 05/11/2021.

[11] Ma Y, Jue ML, Zhang F, Mathias R, Jang HY, Lively RP. Creation of well-defined "mid-sized" micropores in carbon molecular sieve membranes. Angew Chem Sep. 16, 2019;131(38):13 393–413 399. issn: 0044-8249, 1521-3757. doi: 10.1002/ange.201903105. [Online]. Available: https://onlinelibrary.wiley.com/doi/abs/10.1002/ange.201903105. visited on 03/29/2021.

[12] Zhang C, Koros WJ. Ultraselective carbon molecular sieve membranes with tailored synergistic sorption selective properties. issn: 1521-4095 Adv Mater 2017;29(33):1 701–631. https://doi.org/10.1002/adma.201701631 [Online]. Available: https://onlinelibrary.wiley.com/doi/abs/10.1002/adma.201701631. visited on 08/14/2023.

[13] Qiu W, Vaughn J, Liu G, Xu L, Brayden M, Martinez M, Fitzgibbons T, Wenz G, Koros WJ. Hyperaging tuning of a carbon molecular-sieve hollow fiber membrane with extraordinary gas-separation performance and stability

[Online]. Available: Angew Chem Int Ed 2019;58(34):11 700–711 703. https://onlinelibrary.wiley.com/doi/abs/10.1002/anie.201904913. visited on 08/14/2023.
[14] He X, Kumakiri I. Chapter 1 - fundamentals of carbon membranes. In: Carbon membrane technology: fundamentals and applications, Google-books-ID: 05UBEAAAQBAJ. CRC Press; 2020. p. 3–20. isbn: 978-0-429-82034-2.
[15] Lagorsse S, Magalhães F, Mendes A. Xenon recycling in an anaesthetic closed-system using carbon molecular sieve membranes. J Membr Sci Sep. 1, 2007;301:29–38. https://doi.org/10.1016/j.memsci.2007.05.032.
[16] Yang Z, Guo W, Mahurin SM, Wang S, Chen H, Cheng L, Jie K, Meyer HM, Jiang D-e, Liu G, Jin W, Popovs I, Dai S. Surpassing robeson upper limit for CO2/n2 separation with fluorinated carbon molecular sieve membranes. issn: 2451-9294. doi: 10.1016/j.chempr.2019.12.006. [Online]. Available: Chem Mar. 12, 2020;6(3):631–45. https://www.sciencedirect.com/science/article/pii/S2451929419305534. visited on 12/16/2022.
[17] Ngamou PHT, Ivanova ME, Guillon O, Meulenberg WA. High-performance carbon molecular sieve membranes for hydrogen purification and pervaporation dehydration of organic solvents. J Mater Chem A Mar. 19, 2019;7(12):7082–91. Publisher: The Royal Society of Chemistry, issn: 2050-7496. doi: 10.1039/C8TA09504C. [Online]. Available: https://pubs.rsc.org/en/content/articlelanding/2019/ta/c8ta09504c. visited on 08/14/2023.
[18] Koros WJ, Zhang C. Materials for next-generation molecularly selective synthetic membranes. Nat Mater Mar. 2017;16(3):289–97. Number: 3 Publisher: Nature Publishing Group, issn: 1476-4660. doi: 10.1038/nmat4805. [Online]. Available, https://www.nature.com/articles/nmat4805. visited on 08/14/2023.
[19] Saufi SM, Ismail AF. Fabrication of carbon membranes for gas separation—-a review. Carbon Jan. 1, 2004;42(2):241–59. issn: 0008-6223. doi: 10.1016/j.carbon.2003.10.022. [Online]. Available: https://www.sciencedirect.com/science/article/pii/S0008622303005104. visited on 08/14/2023.
[20] Hägg M-B, Lie JA, Lindbråthen A. Carbon molecular sieve membranes: a promising alternative for selected industrial applications. Ann N Y Acad Sci Mar. 2003;984:329–45. https://doi.org/10.1111/j.1749-6632.2003.tb06010.x. issn: 0077-8923.
[21] Sahin Z, Emmery D, Mamaghani AR, Gazzani M, Gallucci F. Mass transport in carbon membranes. Current Opinion in Chemical Engineering Mar. 1, 2023;39:100–896. issn: 2211-3398. doi: 10.1016/j.coche.2022.100896. [Online]. Available: https://www.sciencedirect.com/science/article/pii/S221133982200106X. visited on 02/20/2023.
[22] Gilron J, Soffer A. Knudsen diffusion in microporous carbon membranes with molecular sieving character. J Membr Sci Nov. 15, 2002;209(2):339–52. issn: 0376-7388. doi: 10.1016/S0376-7388(02)00074-1. [Online]. Available: https://www.sciencedirect.com/science/article/pii/S0376738802000741. visited on 05/03/2021.
[23] Rungta M, Xu L, Koros WJ. Structure–performance characterization for carbon molecular sieve membranes using molecular scale gas probes. Carbon Apr. 1, 2015;85:429–42. issn: 0008-6223. doi: 10.1016/j.carbon.2015.01.008. [Online]. Available: https://www.sciencedirect.com/science/article/pii/S0008622315000159. visited on 05/11/2021.
[24] Kruse N, Schießer Y, Kämnitz S, Richter H, Voigt I, Braun G, Repke JU. Carbon membrane gas separation of binary CO2 mixtures at high pressure. Separ Purif Technol 2016;164:132–7. issn: 1383-5866. doi: 10.1016/j.seppur.2016.03.035. [Online]. Available: https://www.sciencedirect.com/science/article/pii/S138358661630140X. visited on 01/21/2022.
[25] Kruse N, Schießer Y, Reger-Wagner N, Richter H, Voigt I, Braun G, Repke J-U. High pressure adsorption, permeation and swelling of carbon membranes – measurements and modelling at up to 20mpa. J Membr Sci Dec. 15, 2017;544:12–7. issn: 0376-7388. doi: 10.1016/j.memsci.2017.09.004. [Online]. Available: https://www.sciencedirect.com/science/article/pii/S0376738817318161. visited on 05/06/2021.
[26] Al-Rabiah AA, Ajbar AM, Soliman MA, Almalki FA, Abdelaziz OY. Modeling of nitrogen separation from natural gas through nanoporous carbon membranes. J Nat Gas Sci Eng Sep. 1, 2015;26:1278–84. issn: 1875-5100. doi: 10.1016/j.jngse.2015.08.040. [Online]. Available: https://www.sciencedirect.com/science/article/pii/S1875510015301050. visited on 05/06/2021.
[27] Rehfeldt S, Stichlmair J. Measurement and calculation of multicomponent diffusion coefficients in liquids. Fluid Phase Equilibria, 16th Symposium on Thermophysical Properties Aug. 1, 2007;256(1):99–104. issn: 0378-3812. doi: 10.1016/j.fluid.2006.10.008. [Online]. Available: https://www.sciencedirect.com/science/article/pii/S0378381206004353. visited on 07/18/2022.
[28] Rangarajan R, Mazid MA, Matsuura T, Sourirajan S. Permeation of pure gases under pressure through asymmetric porous membranes. membrane characterization and prediction of performance. Ind Eng Chem Process Des Dev Jan. 1984;23(1):79–87. issn: 0196-4305, 1541-5716. doi: 10.1021/i200024a014. [Online]. Available: https://pubs.acs.org/doi/abs/10.1021/i200024a014. visited on 12/15/2021.
[29] Li K. Transport and separation of gases in porous ceramic membranes. In: Ceramic membranes for separation and reaction, Section: 4. John Wiley & Sons, Ltd; 2007. p. 97–134. isbn: 978-0-470-31947-5. doi: 10.1002/9780470319475.ch4. [Online]. Available: https://onlinelibrary.wiley.com/doi/abs/10.1002/9780470319475.ch4. visited on 07/02/2021.
[30] Pirouzfar V, Omidkhah MR. Mathematical modeling and optimization of gas transport through carbon molecular sieve membrane and determining the model parameters using genetic algorithm. Iran Polym J (Engl Ed) Mar. 1, 2016;25(3):203–12. https://doi.org/10.1007/s13726-016-0414-z. issn: 1735-5265 visited on 05/10/2021.
[31] Fowlkes JD, Fletcher BL, Hullander ED, Klein KL, Hensley DK, Melechko AV, Simpson ML, Doktycz MJ. Tailored transport through vertically aligned carbon nanofibre membranes; controlled synthesis, modelling, and passive diffusion experiments. Publisher: IOP Publishing, issn: 0957-4484. doi: 10.1088/0957-4484/16/12/063. [Online]. Available: Nanotechnology Nov. 2005;16(12):3101–9. https://doi.org/10.1088/0957-4484/16/12/063. visited on 05/06/2021.
[32] Hankel M, Zhang H, Nguyen TX, Bhatia SK, Gray SK, Smith SC. Kinetic modelling of molecular hydrogen transport in microporous carbon materials. Phys Chem Chem Phys 2011;13(17):7834–44. Publisher: Royal Society of Chemistry. doi: 10.1039/C0CP02235G. [Online]. Available: https://pubs.rsc.org/en/content/articlelanding/2011/cp/c0cp02235g. visited on 05/06/2021.
[33] Jiao Y, Du A, Hankel M, Smith SC. Modelling carbon membranes for gas and isotope separation. Phys Chem Chem Phys Mar. 13, 2013;15(14):4832–43. Publisher: The Royal Society of Chemistry, issn: 1463-9084. doi: 10.1039/C3CP44414G. [Online]. Available: https://pubs.rsc.org/en/content/articlelanding/2013/cp/c3cp44414g. visited on 04/29/2021.
[34] Seo YG, Kum GH, Seaton NA. Monte Carlo simulation of transport diffusion in nanoporous carbon membranes. J Membr Sci Jan. 1, 2002;195(1):65–73. issn: 0376-7388. doi: 10.1016/S0376-7388(01)00549-X. [Online]. Available: https://

www.sciencedirect.com/science/article/pii/S037673880100549X. visited on 07/18/2022.
[35] Xu L, Sedigh MG, Tsotsis TT, Sahimi M. Nonequilibrium molecular dynamics simulation of transport and separation of gases in carbon nanopores. II. binary and ternary mixtures and comparison with the experimental data. J Chem Phys Jan. 8, 2000;112(2):910–22. Publisher: American Institute of Physics, issn: 0021-9606. doi: 10.1063/1.480618. [Online]. Available: https://aip.scitation.org/doi/10.1063/1.480618. visited on 07/18/2022.
[36] Vieira-Linhares AM, Seaton NA. Non-equilibrium molecular dynamics simulation of gas separation in a microporous carbon membrane. Chem Eng Sci Sep. 1, 2003;58(18):4129–36. issn: 0009-2509. doi: 10.1016/S0009-2509(03)00304-X. [Online]. Available: https://www.sciencedirect.com/science/article/pii/S000925090300304X. visited on 07/18/2022.
[37] Chambre PA, Schaaf SA. Flow of rarefied gases. Princeton University Press; 1961. Publication Title: Flow of Rarefied Gases, isbn: 978-1-4008-8580-0. doi: 10.1515/9781400885800. [Online]. Available: https://www.degruyter.com/document/doi/10.1515/9781400885800/html. visited on 09/14/2021.
[38] Uhlhorn R, Keizer K, Burggraaf A. Gas transport and separation with ceramic membranes. part II: synthesis and separation properties of microporous membranes. 1992. https://doi.org/10.1016/0376-7388(92)87017-R.
[39] Kaneko K. Determination of pore size and pore size distribution: 1. adsorbents and catalysts. J Membr Sci Nov. 28, 1994;96(1):59–89. issn: 0376-7388. doi: 10.1016/0376-7388(94)00126-X. [Online]. Available: https://www.sciencedirect.com/science/article/pii/037673889400126X. visited on 09/17/2021.
[40] Park HB, Kim YK, Lee JM, Lee SY, Lee YM. Relationship between chemical structure of aromatic polyimides and gas permeation properties of their carbon molecular sieve membranes. J Membr Sci Feb. 1, 2004;229(1):117–27. issn: 0376-7388. doi: 10.1016/j.memsci.2003.10.023. [Online]. Available: https://www.sciencedirect.com/science/article/pii/S0376738803005258. visited on 08/14/2023.
[41] Hu C-P, Polintan CK, Tayo LL, Chou S-C, Tsai H-A, Hung W-S, Hu C-C, Lee K-R, Lai J-Y. The gas separation performance adjustment of carbon molecular sieve membrane depending on the chain rigidity and free volume characteristic of the polymeric precursor. Carbon Mar. 1, 2019;143:343–51. issn: 0008-6223. doi: 10.1016/j.carbon.2018.11.037. [Online]. Available: https://www.sciencedirect.com/science/article/pii/S0008622318310686 (visited on 08/14/2023).
[42] Llosa Tanco MA, Pacheco Tanaka DA, Mendes A. Composite-alumina-carbon molecular sieve membranes prepared from novolac resin and boehmite. part II: effect of the carbonization temperature on the gas permeation properties. Int J Hydrogen Energy 2015;40(8):3485–96. issn: 0360-3199. doi: 10.1016/j.ijhydene.2014.11.025. [Online]. Available: https://www.sciencedirect.com/science/article/pii/S0360319914031036. visited on 01/18/2022.
[43] Koresh JE, Soffer A. Mechanism of permeation through molecular-sieve carbon membrane. part 1.—the effect of adsorption and the dependence on pressure. J Chem Soc, Faraday Trans 1: Physical Chemistry in Condensed Phases Jan. 1, 1986;82(7):2057–63. Publisher: The Royal Society of Chemistry, issn: 0300-9599. doi: 10.1039/F19868202057. [Online]. Available: https://pubs.rsc.org/en/content/articlelanding/1986/f1/f19868202057. visited on 06/30/2021.
[44] Keizer K, Uhlhorn RJ, Burggraaf TJ. Chapter 12 gas separation using inorganic membranes. In: Membrane science and technology, vol. 2. Elsevier; 1995. p. 553–88. isbn: 978-0-444-81633-7. doi: 10.1016/S0927-5193(06)80014-8. [Online]. Available: https://linkinghub.elsevier.com/retrieve/pii/S0927519306800148. visited on 09/17/2021).
[45] Present RD. Kinetic theory of gases. Third printing edition. McGraw-Hill; Jan. 1, 1958.
[46] Kennard EH. Kinetic theory of gases: with an introduction to statistical mechanics. Incorporated: McGraw-Hill Book Company; 1938. p. 510. pagetotals, Google-Books-ID: uP4gAAAAMAAJ.
[47] Knudsen M. Die gesetze der molekularströmung und der inneren reibungsströmung der gase durch röhren. Ann Phys 1909;333(1):75–130. issn: 00033804, 15213889. doi: 10.1002/andp.19093330106. [Online]. Available: https://onlinelibrary.wiley.com/doi/10.1002/andp.19093330106 (visited on 09/20/2021.
[48] Hwang S-T. Fundamentals of membrane transport. Kor J Chem Eng Jan. 2011;28(1):1–15. issn: 0256-1115, 1975-7220. doi: 10.1007/s11814-010-0493-z. [Online]. Available: http://link.springer.com/10.1007/s11814-010-0493-z. visited on 09/17/2021.
[49] Shelekhin AB, Grosgogeat EJ, Hwang S-T. Gas separation properties of a new polymer/inorganic composite membrane. J Membr Sci Feb. 19, 1992;66(2):129–41. issn: 0376-7388. doi: 10.1016/0376-7388(92)87003-G. [Online]. Available: https://www.sciencedirect.com/science/article/pii/037673889287003G (visited on 10/12/2021).
[50] Hsieh H. Chapter 3 materials and preparation of inorganic membranes. In: Membrane science and technology, vol. 3. Elsevier; 1996. p. 23–92. isbn: 978-0-444-81677-1. doi: 10.1016/S0927-5193(96)80022-2. [Online]. Available: https://linkinghub.elsevier.com/retrieve/pii/S0927519396800222 (visited on 01/17/2022).
[51] Julbe A, Farrusseng D, Guizard C. Porous ceramic membranes for catalytic reactors — overview and new ideas. J Membr Sci Jan. 15, 2001;181(1):3–20. issn: 0376-7388. doi: 10.1016/S0376-7388(00)00375-6. [Online]. Available: https://www.sciencedirect.com/science/article/pii/S0376738800003756 (visited on 09/21/2021).
[52] Hamm JBS, Ambrosi A, Griebeler JG, Marcilio NR, Tessaro IC, Pollo LD. Recent advances in the development of supported carbon membranes for gas separation. Int J Hydrogen Energy Sep. 28, 2017;42(39):24830–45. issn: 0360-3199. doi: 10.1016/j.ijhydene.2017.08.071. [Online]. Available: https://www.sciencedirect.com/science/article/pii/S0360319917332974 (visited on 07/01/2021).
[53] Kong J, Li K. An improved gas permeation method for characterising and predicting the performance of microporous asymmetric hollow fibre membranes used in gas absorption. J Membr Sci Feb. 15, 2001;182(1):271–81. issn: 03767388. doi: 10.1016/S0376-7388(00)00573-1. [Online]. Available: https://linkinghub.elsevier.com/retrieve/pii/S0376738800005731 (visited on 09/16/2021).
[54] Liepmann HW. Gaskinetics and gasdynamics of orifice flow. Publisher: Cambridge University Press, issn: 1469-7645, 0022-1120 J Fluid Mech Feb. 1961;10(1):65–79. https://doi.org/10.1017/S002211206100007X [Online]. Available: https://www.cambridge.org/core/journals/journal-of-fluid-mechanics/article/gaskinetics-and-gasdynamics-of-orifice-flow/8BFE938D7AF0A8CCC28B84F92266A24C (visited on 09/22/2021).
[55] Uhlhorn RJR, Burggraaf AJ. Gas separations with inorganic membranes. isbn: 978-94-011-6547-1. doi: 10.1007/978-94-011-6547-16. [Online]. In: Bhave RR, editor. Inorganic membranes synthesis, characteristics and applications. Dordrecht: Springer Netherlands; 1991. p. 155–76. https://doi.org/10.1007/978-94-011-6547-1_6 (visited on 07/01/2021).
[56] Gilliland ER, Baddour RF, Russell JL. Rates of flow through microporous solids. issn: 1547-5905. doi: 10.1002/aic.690040117. [Online]. Available: AIChE J 1958;4(1):90–6. https://aiche.onlinelibrary.wiley.com/doi/abs/10.1002/aic.690040117 (visited on 07/22/2021).

[57] Weaver JA, Metzner AB. The surface transport of adsorbed molecules. issn: 1547-5905. doi: 10.1002/aic.690120409. [Online]. Available: AIChE J 1966;12(4):655–61. https://onlinelibrary.wiley.com/doi/abs/10.1002/aic.690120409 (visited on 09/27/2021).

[58] Ponzi M, Papa J, Rivarola JBP, Zgrablich G. On the surface diffusion of adsorbable gases through porous media. issn: 1547-5905. doi: 10.1002/aic.690230319. [Online]. Available: AIChE J 1977;23(3):347–52. https://onlinelibrary.wiley.com/doi/abs/10.1002/aic.690230319 (visited on 09/27/2021).

[59] Ash R, Barrer RM, Pope CG. Flow of adsorbable gases and vapours in a microporous medium, II. binary mixtures. Proceedings of the Royal Society of London. Series A. Mathematical and Physical Sciences Jan. 1, 1963;271(1344):19–33. Publisher: Royal Society. doi: 10.1098/rspa.1963.0002. [Online]. Available: https://royalsocietypublishing.org/doi/10.1098/rspa.1963.0002 (visited on 09/27/2021).

[60] Okazaki M, Tamon H, Toei R. Interpretation of surface flow phenomenon of adsorbed gases by hopping model. issn: 1547-5905. doi: 10.1002/aic.690270213. [Online]. Available: AIChE J 1981;27(2):262–70. https://onlinelibrary.wiley.com/doi/abs/10.1002/aic.690270213 (visited on 09/27/2021).

[61] Choi J-G, Do DD, Do HD. Surface diffusion of adsorbed molecules in porous media: monolayer, multilayer, and capillary condensation regimes. Ind Eng Chem Res Sep. 1, 2001;40(19):4005–31. Publisher: American Chemical Society, issn: 0888-5885. doi: 10.1021/ie010195z. [Online].(visited on 03/02/2021).

[62] Seidel A, Carl PS. The concentration dependence of surface diffusion for adsorption on energetically heterogeneous adsorbents. Chem Eng Sci Jan. 1, 1989;44(1):189–94. issn: 0009-2509. doi: 10.1016/0009-2509(89)85244-3. [Online]. Available: https://www.sciencedirect.com/science/article/pii/0009250989852443 (visited on 01/13/2022).

[63] Kapoor A, Yang RT. Surface diffusion on energetically heterogeneous surfaces. issn: 1547-5905. doi: 10.1002/aic.690351019. [Online]. Available AIChE J 1989;35(10):1735–8. https://aiche.onlinelibrary.wiley.com/doi/abs/10.1002/aic.690351019. visited on 07/01/2021.

[64] A. Kapoor and R.T. Yang, "Surface diffusion on energetically heterogeneous surfaces—an effective medium approximation approach," Chem Eng Sci, vol. 45, no. 11, pp. 3261–3270, Jan. 1, 1990, issn: 0009-2509. doi: 10.1016/0009-2509(90)80218-4. [Online]. Available: https://www.sciencedirect.com/science/article/pii/0009250990802184 (visited on 07/01/2021).

[65] Lee K-H, Hwang S-T. The transport of condensible vapors through a microporous vycor glass membrane. J Colloid Interface Sci Apr. 1, 1986;110(2):544–55. issn: 0021-9797. doi: 10.1016/0021-9797(86)90407-8. [Online]. Available: https://www.sciencedirect.com/science/article/pii/0021979786904078 (visited on 09/30/2021).

[66] Poto S, Endepoel JGH, Llosa-Tanco MA, Pacheco-Tanaka DA, Gallucci F, Neira d'Angelo MF. Vapor/gas separation through carbon molecular sieve membranes: experimental and theoretical investigation. Int JHydrog Energy, Sustain Hydrog Energy Technol Mar. 8, 2022;47(21):11385–401. issn: 0360-3199. doi: 10.1016/j.ijhydene.2021.10.155. [Online]. Available: https://www.sciencedirect.com/science/article/pii/S0360319921042129 (visited on 05/13/2023).

[67] Coasne B, Galarneau A, Pellenq RJM, Renzo FD. Adsorption, intrusion and freezing in porous silica: the view from the nanoscale. Chem Soc Rev Apr. 16, 2013;42(9):4141–71. Publisher: The Royal Society of Chemistry, issn: 1460-4744. doi: 10.1039/C2CS35384A. [Online]. Available: https://pubs.rsc.org/en/content/articlelanding/2013/cs/c2cs35384a (visited on 09/12/2022).

[68] Coasne B. Multiscale adsorption and transport in hierarchical porous materials. New J Chem May 10, 2016;40(5):4078–94. Publisher: The Royal Society of Chemistry, issn: 1369-9261. doi: 10.1039/C5NJ03194J. [Online]. Available: https://pubs.rsc.org/en/content/articlelanding/2016/nj/c5nj03194j (visited on 09/12/2022).

[69] Choi B-U, Choi D-K, Lee Y-W, Lee B-K, Kim S-H. Adsorption equilibria of methane, ethane, ethylene, nitrogen, and hydrogen onto activated carbon. J Chem Eng Data Mar. 18, 2003;48(3):603–7. Publisher: American Chemical Society, issn: 0021-9568. doi: 10.1021/je020161d. [Online]. (visited on 12/03/2021).

[70] Bénard P, Chahine R. Determination of the adsorption isotherms of hydrogen on activated carbons above the critical temperature of the adsorbate over wide temperature and pressure ranges. Langmuir Mar. 1, 2001;17(6):1950–5. Publisher: American Chemical Society, issn: 0743-7463. doi: 10.1021/la001381x. [Online]. (visited on 11/22/2021).

[71] Bell JG, Benham MJ, Thomas KM. Adsorption of carbon dioxide, water vapor, nitrogen, and sulfur dioxide on activated carbon for capture from flue gases: competitive adsorption and selectivity aspects. Energy Fuels May 6, 2021;35(9):8102–16. Publisher: American Chemical Society, issn: 0887-0624. doi: 10.1021/acs.energyfuels.1c00339. [Online]. (visited on 04/21/2022).

[72] Saha BB, Jribi S, Koyama S, El-Sharkawy II. Carbon dioxide adsorption isotherms on activated carbons. J Chem Eng Data May 12, 2011;56(5):1974–81. Publisher: American Chemical Society, issn: 0021-9568. doi: 10.1021/je100973t. [Online]. (visited on 07/25/2022).

[73] Rahimalimamaghani A, Pacheco Tanaka DA, Pacheco Tanaka DA, Llosa Tanco MA, Neira D'Angelo F, Gallucci F. Effect of aluminium acetyl acetonate on the hydrogen and nitrogen permeation of carbon molecular sieves membranes. Int J Hydrogen Energy Apr. 15, 2022;47(32):14570–9. issn: 0360-3199. doi: 10.1016/j.ijhydene.2022.02.198. [Online]. Available: https://www.sciencedirect.com/science/article/pii/S0360319922008655 (visited on 04/29/2022).